

**Experimental Studies on Terahertz Backward Wave
Oscillator Driven by Weakly Relativistic Electron Beam**

Dissertation in Electrical and Information Engineering submitted to the Graduate School of Science and Technology of Niigata University in partial fulfillment of the requirements for the degree of Doctor of Philosophy

By

Gong Shaoyan

Graduate school of Science and Technology

Niigata University

March 2016

Contents

1	INTRODUCTION AND BASIC TECHNIQUES OF BACKWARD WAVE OSCILLATORS	
1.1	Introduction	• • • 5
1.2	Purpose of Research	• • • 7
1.3	Outline of the Dissertation	• • • 9
2	G-BAND SLOW WAVE STRUCTURE	
2.1	Introduction	• • • 10
2.1.1	Beam mode	• • • 10
2.1.2	Cherenkov interaction	• • • 10
2.1.3	Slow wave structure	• • • 11
2.2	G-band Slow Wave Structure	• • • 11
2.2.1	G-band BWO	• • • 11
2.2.2	G-band CSW-resonator	• • • 12
2.3	Dispersion Relation	• • • 14
2.3.1	Dispersion relation of the G-band BWOs	• • • 18
2.3.2	Dispersion relation of the G-band CSW-resonator	• • • 19
2.4	Summary and Discussion	• • • 22
3	ELECTRON BEAM AND CATHODE	
3.1	Electron Beam	• • • 23
3.2	Electron Beam Diode	• • • 23
3.3	Cathode	• • • 24
3.4	Burn Pattern of Electron Beam	• • • 24
3.5	Beam Generation	• • • 25
3.6	Principle of Electron Emission	• • • 26
3.6.1	Explosive electron emission	• • • 27
3.6.2	Field-enhancement EEE	• • • 27
3.6.3	Surface-flashover EEE	• • • 28
3.7	Summary and Discussion	• • • 28
4	EXPERIMENTAL STUDIES ON G-BAND BACKWARD WAVE OSCILLATOR AND CYLINDRICAL SURFACE WAVE RESONATOR	

4.1	Experimental Setup	• • • 30
4.1.1	Marx generator	• • • 31
4.1.2	Pulse forming line	• • • 31
4.1.3	Guiding magnetic field	• • • 33
4.1.4	Vacuum device	• • • 35
4.1.5	Rogowski coil	• • • 35
4.1.6	Microwave detection system	• • • 36
4.2	Frequency Measuring Experiment	• • • 36
4.2.1	G-band BWO	• • • 36
4.2.2	G-band CSW-resonator	• • • 37
4.3	Microwave Oscillation Experiment	• • • 37
4.3.1	G-band BWO	• • • 37
4.3.2	G-band CSW-resonator	• • • 38
4.4	Microwave Power versus SWS Length	• • • 39
4.4.1	G-band BWO	• • • 39
4.4.2	G-band CSW-resonator	• • • 40
4.5	Radiation Pattern of The Output Microwaves	• • • 42
4.5.1	G-band BWO	• • • 42
4.5.2	G-band CSW-resonator	• • • 44
4.6	Summary and Discussion	• • • 45

5 THEORETICAL AND EXPERIMENTAL STUDIES ON STARTING ENERGY AND CURRENT FOR OSCILLATION

5.1	Starting Energy for Oscillation	• • • 47
5.1.1	Numerical analysis and estimation of the starting energy for G-band BWO oscillation	• • • 47
5.1.2	Numerical analysis and estimation of the starting energy for G-band CSW-resonator	• • • 51
5.2	Starting Current for Oscillation	• • • 55
5.2.1	Numerical analysis of starting current	• • • 55
5.2.2	Experiment of the starting current for K-band BWO oscillation	• • • 56
5.3	Summary and Discussion	• • • 60

6 CONCLUSIONS

ABSTRACT

In this dissertation, the results of theoretical and experimental studies on a vacuum backward wave oscillator (BWO) and cylindrical surface waves (CSWs) resonator are presented. Slow-wave devices such as backward wave oscillator (BWO) have been studied extensively as a candidate for high or moderate power microwave sources. In BWOs, slow-wave structure (SWS) is used to form slow wave by reducing the phase velocity of electromagnetic wave to the beam velocity. To increase the operation frequency and the power handling capability, the diameter D of SWS is increased larger than the free-space wavelength λ of output electromagnetic wave, i.e. $D/\lambda > 1$. In oversized cases, the slow wave becomes a surface wave concentrated on SWS wall. The designed BWOs and CSW-resonators are with upper cut off frequencies in the modern IEEE G-band (110-300GHz). The G-band SWS used in this work is an oversized hollow waveguide and a metal cylinder with periodical corrugations as G-band BWO and CSW-resonator. The corrugation parameters are the average radius R_0 , corrugation width d , periodic length z_0 , and corrugation amplitude h . The radius R_0 is the center point between the top and bottom of the corrugation. The corrugation wavenumber is given by $k_0 = 2\pi/z_0$. The dispersion characteristics of CSW are determined by changing R_0 , h , d , and z_0 . Dispersion curves of the CSW are obtained by a numerical method based on a modal expansion of the electromagnetic field for corrugated feed-horns. We have been studying oversized BWOs driven by a weakly relativistic beam of less than 100kV. The beam is generated by a disk cold cathode and the propagation of the electron beam has been investigated in detail. The intense radiations in terahertz region based on the BWO and CSW-resonator are reported.

We examine the starting conditions for intense G-band BWO and CSW-resonator operation by varying the beam parameters and SWS lengths. There are two threshold conditions for such intense radiations. One is the well-known starting current, which is common in many microwave sources. The other is a starting energy, whose existence has been pointed out for the non-oversized X-band BWO and the oversized K-band BWO. It is shown that a starting energy exists for the G-band BWO and CSW-resonator which is more critical than the starting current in the oversized BWOs. We estimated the starting energy for G-band BWOs oscillation by numerical analysis and the experimental obtained starting energy values are in excellent agreement with the calculated ones. Above the starting energy, very intense output powers on the order of kW are obtained. The figure of merit Pf^2 is on the order of $10^5 \text{ kW} \cdot \text{GHz}^2$ and nearly the same as that for the K- and Q-band BWOs. The oscillation-starting condition for such intense operation may play an important role in high-intensity terahertz wave sources.

ACKNOWLEDGMENTS

Acknowledgements my deepest gratitude goes first and foremost to advisory Professor Kazuo Ogura for his congenial support and invaluable advice during the course of this research work. He has walked me through all the stages of the writing of this dissertation. He has given me lots of useful advices on my writing, and has tried his best to improve this dissertation. His timely advice and proper guidance make it possible to complete the present dissertation in the expected time. Second, I would like to express my heartfelt gratitude to Professor Kiyoyuki Yambe, Professor Akira Sugawara, Mr. Shota Magori, Mr. Takauki Iwasaki, who have instructed and helped me a lot in the past three years. Without their consistent and illuminating instructions, this dissertation could not have reached its present form.

The author would like to acknowledge the support from the NIFS collaboration research programs No.NIFS12KLER014 and No. NIFS14KLER031. The authors gratefully acknowledge the invaluable discussions with Professors Sin Kubo and Takashi Shimosuma, the National Institute for Fusion Science, Japan. We also thank Sakuji Kobayashi and Kohji Okada for their assistance in designing and fabricating the corrugation.

The author is indebted to all of the members of the Lab. for their kind cooperation and stimulating technical discussions.

The author is particularly grateful to his parents for their eternal love and encouragements.

Finally, the author would like to thank to all individuals in department of Electrical and Information Engineering and Graduate School of School of Science and Technology, Niigata University.

1 INTRODUCTION AND BASIC TECHNIQUES OF BACKWARD WAVE OSCILLATORS

1.1 Introduction

High-Power microwave (HPM) sources are important for a number of advanced applications ranging from the current drive and RF heating of magnetically confined plasmas in fusion devices to high-resolution nanosecond radars [1]-[3]. Many different HPM sources utilizing electron beams have been developed over the past few decades. The basic idea of the generation of microwave radiation from the velocity modulation and bunching of the beam was developed since klystron and magnetron were invented in the mid-1930s [4]. During the Second World War, a strong microwave became necessary for radar systems, traveling-wave tube (TWT) and backward wave oscillator (BWO) were developed. In the late 1950s, an experiment of gyrotron has begun to be done. The development of high- power gyrotron since 1960s was motivated primarily by the application the heating and control of magnetically confined fusion plasma [5]. The gyrotrons have made it possible to produce short wavelength radiation (so-called millimeter waves). The development of pulsed power technology in the late 1960s provided the ability to generate intense relativistic electron beam. The availability of intense relativistic electron beam enabled to generate HPM from Cherenkov devices such as the dielectric Cherenkov maser, TWT and BWO.

Slow wave devices such as the backward wave oscillator (BWO) have been around since the early 1950s [6]. Consisting of a linear electron beam propagated through a spatially periodic slow wave structure (SWS), the BWO possesses a number of desirable features, including high spectral purity, frequency tenability, and the ability to produce relatively high output power. Typically, the diameter of the device is on the order of a free space electromagnetic wavelength. Relativistic BWOs with non-oversized ($D/\lambda \sim 1$) slow wave structures have produced output powers in the 100-1000 MW range at frequencies ranging from 3-15 GHz [7], [8].

Internal breakdown due to field emission from conducting surfaces is a key factor which limits the maximum power output from all high power devices. One method of increasing the power handing capability of a given class of device is to use an oversized structure, increasing the diameter of the electrodynamic structure to several times a free space electromagnetic wavelength. In this manner, microwave generating structures may be designed with resulting internal RF electric fields below critical breakdown levels. Potential detrimental consequences of this oversized design approach, however, include mode competition, mode conversion, and a

general broadening of the frequency spectrum – all factors which can contribute to a decrease in RF power generation efficiency.

In slow-wave devices, a slow-wave structure (SWS) is used to reduce the phase velocity of the electromagnetic wave to the beam velocity. To increase the operation frequency and power-handling capability, oversized devices have been used successfully [9], [10]. The term “oversized” means that the diameter D of the SWS is at least several times larger than the free-space wavelength λ of output electromagnetic wave. In oversized cases, the slow-wave becomes a surface wave concentrated on the SWS wall. The relativistic diffraction generator and the multiwave Cherenkov generator are special versions of oversized BWOs and have produced peak powers of GW orders at frequencies of up to about 46 GHz (Q-band) [11], [12]. The performance of weakly relativistic oversized BWOs has also been improved in K- and Q-bands [10], [13]; radiation powers of up to 500 kW (K-band) and 200 kW (Q-band) have been demonstrated.

Electromagnetic wave sources consisting of a metal grating and electron beam have been studied extensively as the candidates for intense wave sources in the visible, far-infrared and terahertz region. Such devices include Smith-Purcell free electron laser (SP-FEL) [14], Orotron [15], Ledatron [16], traveling wave tubes (TWT) [17], and backward wave oscillator (BWO) [18]. In SP-FELs, electron beams pass near the grating and excite some of the spatial harmonics of grating in the fast-wave region leading to SP radiations [14]. The original SP radiations are spontaneous and essentially weak. Recently, “super-radiance” due to stimulated SP radiation has been reported [19] and enhancement of the SP radiation has been extensively studied [20]-[23]. The resonant interaction of beam with the surface wave is essential to the SP radiation power enhancement.

The SP-FELs described above are commonly based on a planar geometry. Another realistic geometry is cylindrical one, which has been used for high-power BWOs. The slow-wave structures (SWSs) of BWOs can form slow waves with the phase velocity that is close to the beam velocity. To increase the operation frequency and the power handling capability, SWSs are oversized with the diameter D , which is larger than the free-space wavelength λ of output electromagnetic wave, i.e., $D/\lambda > 1$. The slow waves in oversized SWS are surface waves concentrated in the vicinity of the walls like SP-FELs. Performance of the weakly relativistic oversized BWO has been improved by using uniformly distributed annular electron beam of current on the order of 100 A [10], [24]. Hence, an idea of SP-FEL incorporating oversized cylindrical SWS seems to be attractive for the improvement of the radiation intensity [25], [26].

From the point of view of electromagnetic metamaterials, the grating or the corrugated wall is a surface with sub-wavelength structures. Pendry *et al.* discussed electromagnetic fields on a structured planar perfect conductor and pointed out that the structured surface forms surface

plasmon polariton-like (SPP-like) bound states and hybrid surface plasmons [27]. And the highly confined guiding of the SPP-like waves has been verified using a planar plasmonic metamaterial [28]. In a cylindrical geometry, the boundary condition on the side ends of a planar grating [29] is replaced by an azimuthally periodic condition in the cylindrical coordinate system, leading to axisymmetric and non-axisymmetric cylindrical surface waves (CSWs), i.e., cylindrical SPPs [30], [31]. Since the CSWs are clinging to the cylinder and are reflected at the corrugation ends, they form a resonator in the same way as the conventional waveguide cavity. We refer this resonator as CSW-resonator. Electromagnetic properties of resonator can be examined based on a cavity resonance method, in which the microwave reflection and/or transmission are measured as a function of frequency by a network analyzer [32]. This method has been successfully applied to examine a CSW-resonator in the microwave region [33], in which a K-band CSW-resonator is excited by needle antennas placed coaxially. The obtained resonance curves show that the CSWs are classified into two types. One is “bounded surface wave” around the upper cut off, in other words, border of the first Brillouin zone. The other is “hybrid surface wave” in the region away from the upper cut off. The latter has similar properties as the Sommerfeld wave on a smooth metal wire [34]. The two correspond to SPP-like bound state and hybrid surface plasmon in the planar case.

In this dissertation, two classes of oversized high power microwave generators are studied: (1) An oversized G-band backward wave oscillator consisting of a periodically corrugated slow wave structure; and (2) a G-band CSW-resonator formed on the rectangularly corrugated cylindrical wall with parameters used in an intense terahertz BWO.

1.2 Purpose of Research

High-power microwave source can be classified by the phase velocity of the electromagnetic waves which interact with the electron beam. When the phase velocity is faster than the speed of light the microwave source is called fast-wave microwave source, e.g. Gyrotron, on the other hand it is called slow-wave microwave source, e.g. backward wave oscillator.

Over the past twenty years the terahertz (THz) frequency range (30 GHz~3 THz) is very attractive for a number of research and technical applications. Many groups in different countries have focused their efforts on development and elaboration of THz technique and its applications to various problems. The most promising and vast fields of applications include spectroscopy, imaging, space exploration, covert communications, compact radar ranges, industrial controls, terahertz microscopy, terahertz tomography, homeland security, diagnostics of complex media, medical and biological applications based on three points as following:

- (1) THz radiation can detect concealed weapons since many non-metallic, non-polar materials are transparent to THz radiation.

(2) Target compounds such as explosives and illicit drugs have characteristic THz spectra that can be used to identify these compounds.

(3) THz radiation poses no health risk for scanning of people.

With the advancement of THz technologies, THz sensing and imaging will impact a broad range of interdisciplinary fields, including chemical and biological detections and identifications. In particular, THz radiation offers the opportunity for transformational advances in defense and security.

Today there exist several sources of coherent radiation of the THz frequency range, including backward wave oscillators (BWOs) [35], [36] travelling wave tubes (TWTs) [35], gyrotrons [37]-[39], orotrons [40], and free electron lasers (FELs) [41], [42].

BWOs are slow wave device where the electrons spiralize through a corrugated structure in an axial magnetic field interacting with the first spatial harmonic of the backward wave. Indeed, in this region of the dispersion relation, the phase velocity of the wave is positive and the group velocity is negative. They can be tuned over tens of GHz by varying the accelerating potential.

Gyrotrons as fast-wave microwave source have been studied for high-frequency heating in the fusion field. Moreover, in order to use the energy of the electrons in the vertical direction and generate a strong magnetic field such like intense superconducting magnets the accelerator and large-scale devices are necessary.

Free electron lasers (FELs) are known as tunable sources of high power THz radiation, which provide even higher frequencies and pulsed power than gyrotrons. But they are large scale, high cost and do not have the necessary frequency stability for laboratory or field applications.

In our research, a table-top terahertz backward wave oscillator (BWO) driven by weakly relativistic electron beam has been studied for use in the terahertz range. BWO has been chosen as our THz source device for its special features such as high output power, good wave-front quality, good stability, and wavelength tenability. Moreover, comparing with the other similar devices, the main advantages of the BWOs are portability and low cost due to not having to use either a strong magnetic field or a large accelerator facility. For oscillations, electron beam is incident to the axial direction of the waveguide with slow-wave structure which can be interacted with the electromagnetic fields. The BWO is a more compact and lightweight microwave source device compared with the other free electron based devices, thus it can be expected as a commercially available high intensity THz source in future.

There is a general lack of basic data available to facilitate the understanding of this THz source. The purpose of this dissertation is to examine the oscillation characteristics and carry out a systematic experimental investigation of the oversized G-band BWO and CSW-resonator structures, measuring such critical parameters as RF output power and efficiency as a function of electron beam parameters and structure dimensions, starting oscillation energies and currents.

1.3 Outline of Dissertation

The main objective of this dissertation is to make comprehensive investigation on a high power backward wave oscillator using sinusoidally corrugated metal slow wave structures of conventional and large diameter types. The study has been carried out both theoretically and experimentally. This dissertation is an experimental study of high power microwave generation using two classes of oversized, weakly relativistic electron beam devices: (1) An oversized G-band backward wave oscillator consisting of a periodically corrugated slow wave structure; and (2) a G-band CSW-resonator formed on the rectangularly corrugated cylindrical wall with parameters used in an intense terahertz BWO. The G-band SWS is designed for operation with an electron beam with moderate energy less than 100 keV. The reasons behind the selection of oversized SWS is to obtain high power operation at higher frequencies using an electron beam with moderate energy and to avoid RF breakdown inside the SWS. Although the diameter of the structure is large, other parameters are so selected that the structure will oscillate in THz region. The organization of the dissertation is as follows.

In chapter 2, the G-band slow wave structures have been analyzed. The dispersion relation, Cherenkov interaction and Floquet harmonics for the fundamental and higher axial modes have been analyzed in detail.

In chapter 3, the electron beam generation, electron emission, and cathode using in this work have been introduced in detail.

In chapter 4, the experimental setup and results are reported and discussed in detail.

In chapter 5, the starting conditions for G-band BWO and CSW-resonator have been examined theoretically and experimentally.

In chapter 6, some conclusions for this work are shown.

2 G-BAND SLOW WAVE STRUCTURE

2.1 Introduction

2.1.1 Beam mode

HPM device utilizes electron beam as an energy source. Generally, in order to control orbit of this electron beam, a guiding magnetic field is used. The electron motion of the beam is restricted in a range of cyclotron motion by guiding magnetic field. Thus, for an electron beam propagating along the direction of a magnetic field, there exist four beam modes, namely; slow and fast space charge modes and slow and fast cyclotron modes. A slope of a cold beam line is given by beam velocity v_0 . The space charge and cyclotron modes are $\omega = k_z v_0 \pm \Omega/\gamma_0$, respectively. Here, γ_0 is a relativistic factor, k_z is wave number, Ω is the angular electron cyclotron frequency and its sign + and - mean, respectively, fast and slow modes. Furthermore, all beam modes receives some displacement due to plasma frequency when the beam current considered. Due to this, the space charge modes are divided into slow and fast modes.

2.1.2 Cherenkov interaction

A Cherenkov interaction occurs due to the resonance between electric field and electron plasma oscillation of the beam. The resonance condition is given by $\omega' \equiv \omega - k_z v_0 = 0$. To generate high-power coherent radiation, electron tubes are used in which free electrons move along a static magnetic field and give their kinetic energy to an EM wave. Cherenkov radiation occurs when electrons move in a dielectric medium with a velocity greater than the phase velocity of the EM wave in the medium. A diagrammatic representation of the processes is shown in Fig. 2.1. Operations of BWO and TWT and magnetrons are based on Cherenkov radiation of electrons interacting with a slow EM wave propagating near the surface of the slow wave structure (SWS). In order to generate the Cherenkov interaction, the SWS is

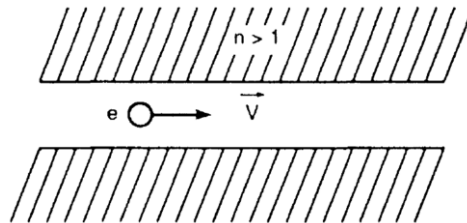


Fig. 2.1. Schematic of Cherenkov radiation. Electron e moves with velocity v through the channel in a dielectric medium with refractive index $n > 1$.

indispensable.

2.1.3 Slow wave structure

When the phase velocity of EM wave mode is reduced to the beam velocity by means of slow wave structures (SWSs), the microwave radiation can occur at frequencies approximately given by intersections between the slow beam modes and the normal EM mode. The electron beam propagates axially through a SWS capable of supporting EM waves with phase velocity v_{ph} , less than the velocity of light c in vacuum. The space charge waves of the beam interact with the normal modes of the SWS and that leads to an instability indispensable for microwave generation.

2.2 G-band Slow Wave Structure

2.2.1 G-band BWO

The G-band BWO used in this work is an oversized hollow waveguide with outer corrugation as shown in Fig. 2.2. The average radius of this corrugated waveguide is 15 mm. The corrugation parameters are the corrugation amplitude h , periodic length z_0 , and corrugation width d . The corrugation wavenumber is given by $k_0 = 2\pi/z_0$. The dispersion characteristics of the structure are controlled by changing h , d , and z_0 . The designed parameters of the G-band rectangular corrugation used in this work are listed in Table 2.1. The parameters of the fabricated corrugation are measured using a digital microscope and are also listed in Table 2.1. By increasing h , the upper cut off frequency decreases. The difference between the designed and fabricated values of h is about 17% and the upper cut off frequency changes from 170 to 150 GHz, a change of about 11%. Compared with the other parameters, the corrugation amplitude h can have a more significant impact on the frequency. Another important factor to be considered in realistic devices is the finiteness of the SWS length L . In our experiment, L takes values of $20z_0$, $40z_0$, and $80z_0$.

		h [mm]	d [mm]	z_0 [mm]
Outer corrugation	Design	0.15	0.3	0.5
	Fabrication	0.175	0.288	0.503

Table. 2.1. Parameters of G-band corrugation.

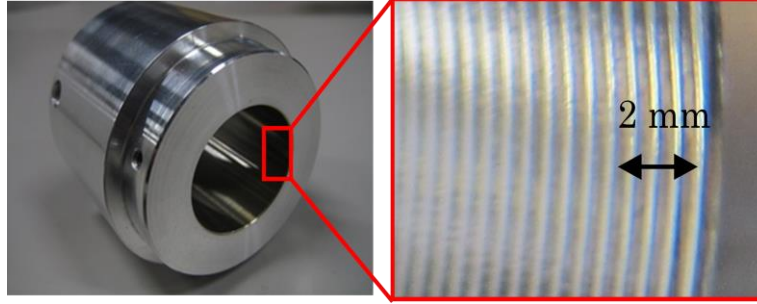


Fig. 2.2. Left: Photograph of G-band corrugated hollow waveguide with length $L= 80z_0$. Right: Enlarged photo of rectangular corrugation.

2.2.2 G-band CSW-resonator

CSW-resonator is formed on a rectangularly corrugated cylinder, whose photograph and cross sectional micrograph are shown in Fig. 2.3 and Fig. 2.4, respectively. The corrugation parameters are the average radius R_0 , corrugation width d , periodic length z_0 , and corrugation amplitude h . The radius R_0 is the center point between the top and bottom of the corrugation and in this work R_0 is 12.6 mm. The corrugation wavenumber is given by $k_0 = 2\pi/z_0$. The dispersion characteristics of CSW are determined by changing R_0 , h , d , and z_0 . In this work, two types of corrugated cylinder with different h are designed, and the parameters of the fabricated corrugation are measured using a digital microscope and are listed in Table 2.2. To prevent the erosion of the corrugation by the high-energy beam, we set a beam limiter at the entrance of the waveguide as shown in Fig. 2.5. The image of the corrugated cylinder inserted into the waveguide is shown in Fig. 2.6. Originally, it is set covered by a waveguide rather than being exposed, in order to facilitate understanding of the internal structure it is not attached to the waveguide but the corrugated cylinder supported with beams limiter at this time.

		h [mm]	d [mm]	z_0 [mm]
Outer corrugation	A-type	0.135	0.3	0.5
	B-type	0.069	0.3	0.5

Table. 2.2. Parameters of G-band CSW-resonators.

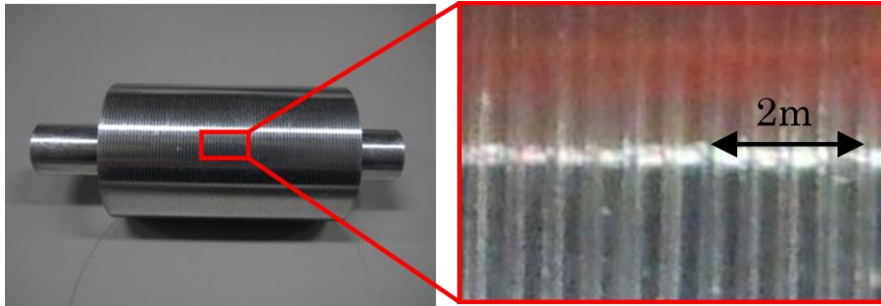


Fig. 2.3. Left: Photograph of a rectangularly corrugated cylinder. Right: Enlarged photo of rectangular corrugation.

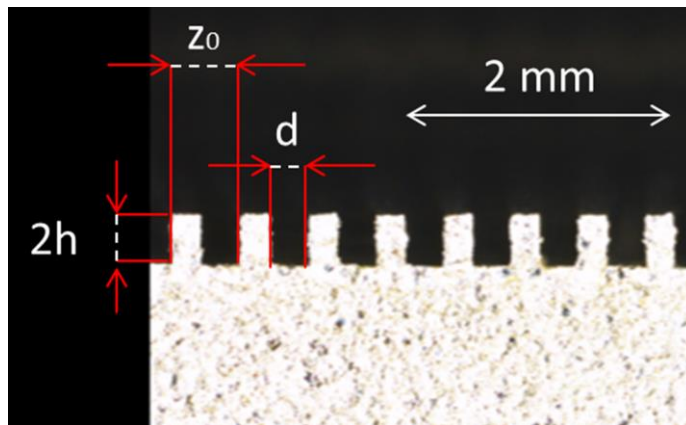


Fig. 2.4. Cross sectional micrograph of periodically corrugated cylinder taken by a digital microscope.



Fig. 2.5. Photograph of beam limiter.



Fig. 2.6. Photograph of internal structure of the waveguide.

2.3 Dispersion Relationship

We consider a very long, large diameter electron beam drifting along the z -axis through a metallic drift tube confined by a strong axial magnetic field, B_0 . The axial bunching of the electrons produces oscillation due to the space charge forces between the electrons, and the bunching consequently develops space charge waves. The dispersion relation of the space charge waves can be expressed by the following equation,

$$\omega = kv \pm \omega_b \gamma^{-3/2} \quad (2.1)$$

where $\omega = (|n_0| e / \epsilon_0 m)^{1/2}$ is the beam plasma angular frequency for the beam with charge density n_0 , k is the axial wavenumber, and axial velocity v with $\gamma = (1 - v^2/c^2)^{-1/2}$, the relativistic factor. Wave with angular frequency ω using '+' sign in (2.1) is usually called the *fast space charge wave* and that with '-' sign is the *slow space charge wave*. However, both waves have $v_{ph} < c$. For finite B_0 , satisfying the cyclotron resonance of the electron Larmor motion, there exist another two modes of electron oscillation, the fast and slow electron cyclotron beam modes. The slow space charge wave is the negative energy wave, which interacts unstably with the slow EM mode of the SWS. When an appropriate condition is satisfied, the structure wave extracts energy from the slow space charge wave of the beam. However, slow space charge wave with $v_{ph} < c$ cannot couple with the normal modes of the smooth-walled waveguide, which have $v_{ph} > c$. In order to achieve the synchronism between slow space charge wave and the structure normal mode, the latter should be slowed down with respect to c . There are various ways of slowing the waveguide modes:

- (1) By inserting dielectric materials with dielectric constant ϵ significantly greater than ϵ_0 , so that the speed of normal mode becomes $c' = c(\epsilon_0/\epsilon)^{1/2}$, which is less than c [43].
- (2) Using disk loaded resonator or by making periodically corrugated structure.
- (3) By filling the waveguide partially fully with dense plasma [44, 45].
- (4) By modifying the space charge dispersion relation. If a periodic transverse magnetic field is applied inside the waveguide, the dispersion curves for the space charge wave will upshift in frequency by an amount $\omega_w \approx k_w v$, where k_w is the axial wavenumber of the magnetic field called wiggler [46]. This is the principle of operation of the FEL.

The periodic corrugation in the inner wall of the waveguide changes the radial and axial boundary conditions for the EM waves. The EM fields in such an SWS are usually represented by the Floquet harmonics. Dominant contributions of far displaced slow space harmonics to EM fields produce the bandpass characteristics in the dispersion diagram for the SWS. When electron beam with finite current propagates through the structure, the slow space charge wave of the beam can synchronize with one of the slow space harmonics of the structure mode. A typical dispersion diagram for sinusoidal corrugated SWS is shown in Fig. 2.7. The operating regions of the various slow wave devices in the ω - k space are indicated in the figure.

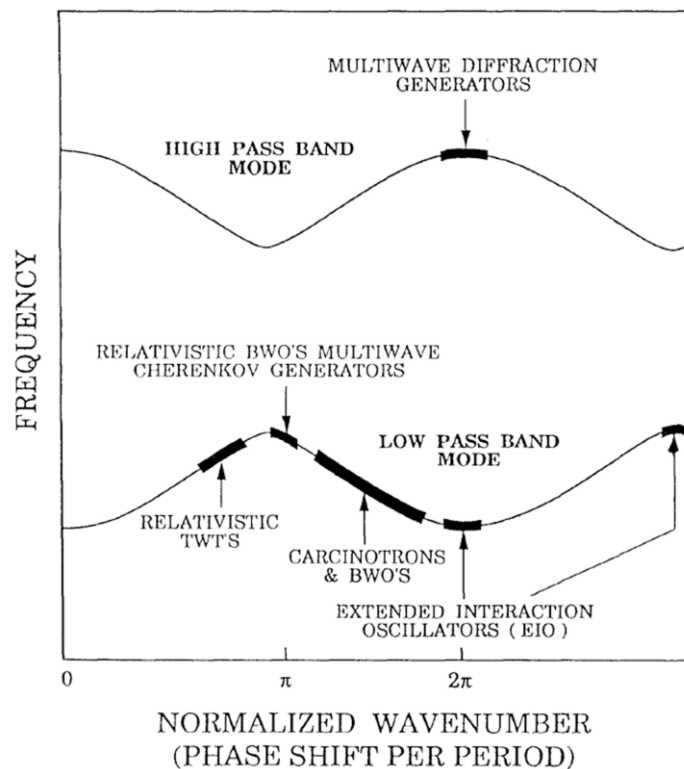


Fig. 2.7. Dispersion curves of a typical SWS. The regions of operation of the various HPM sources are indicated in the figure.

2.3.1 Electromagnetic modes in a periodic SWS

The main function of an SWS is to produce EM fields with $v_{ph} < c$, so that they can interact synchronously with the electron beam. In the devices like BWO's or TWT's, electron beam drifts axially under the guidance of a strong B_0 . The slow space charge wave of the beam couples with the electric field, E_z , of the structure mode. If the beam and the SWS are azimuthally symmetric, the propagating modes with nonzero E_z are the TM modes. Therefore, in such an SWS, only axisymmetric TM modes can be excited by an axially drifting electron beam. Let us consider an infinitely long periodic SWS whose axis coincides with the z -axis, which is also the propagating direction of the beam. The EM fields in such structures can be represented by the well-known Floquet's space harmonics. According to this theorem, the EM quantities at two identical positions separated by one corrugation period, z_0 differs only by a complex constant. Assuming a phase factor of $e^{j(kz-\omega t)}$ for every RF quantity, the electric field in a cylindrical periodic SWS can be expressed in the following form

$$E(r, z, t) = e^{j(kz-\omega t)} E(r, z) \quad (2.2)$$

where ω is the angular frequency and k is the axial wavenumber of the fundamental space harmonic. The spatial field $E(r, z)$ in (2.2) can be written as the sum of Floquet's harmonics in the following way

$$E(r, z, t) = \sum_{n=-\infty}^{\infty} E_{rzn}(r) e^{(2\pi n/z_0)z} \quad (2.3)$$

combining 2.2 and 2.3, we get,

$$E(r, z, t) = \sum_{n=-\infty}^{\infty} E_{rzn}(r) e^{j(kz-\omega t)} \quad (2.4)$$

where $k_n = k + 2\pi n/z_0$. Each of the Floquet harmonics E_{rzn} must satisfy Maxwell's equations with appropriate boundary conditions.

The dispersion relation for the SWS can be obtained by imposing the radial and axial boundary conditions on the field equations. Figure 2.8 and 2.9 show the dispersion diagrams of the lowest order modes for a hypothetical SWS for the spatial harmonics propagating in the z and $-z$ directions, respectively. The complete dispersion diagram can be obtained by superimposing these two figures as shown in Fig. 2.10. The phase velocity of the n 'th spatial harmonic

is $v_{ph} = \omega/k_n = \omega/(k + nK_0)$. For $n = 0$, v_{ph} is the same as that of the straight cylindrical waveguide and equal to c . As the contributions of the other space harmonics increase, the phase velocity decreases and becomes less than c . Thus the EM field equations so far derived are slow wave type and are to interact with the relativistic electron beam. The group velocity $v_g = \delta\omega/\delta k$ is, however, the same for all harmonics. The group velocity of the slow wave may be either positive, zero or negative depending on the wavenumber, k , within the first Brillouin zone of the dispersion curve as can be seen from Fig. 2.10. The shaded portion in the figure represents the region where the phase velocity of the structure wave is less than c . This shaded portion between the frequencies ω_1 and ω_2 of the dispersion diagram represents the region where the slow space charge wave or the beam and the slow structure mode can interact with high efficiency. For a fixed SWS geometry, the beam-wave interaction is controlled by the beam parameters such as energy, space charge and geometrical configuration. If the beam interacts with a spatial harmonic with negative group velocity, an absolute instability will develop and which will consequently produce a growing wave propagating in the direction opposite to that of the beam.

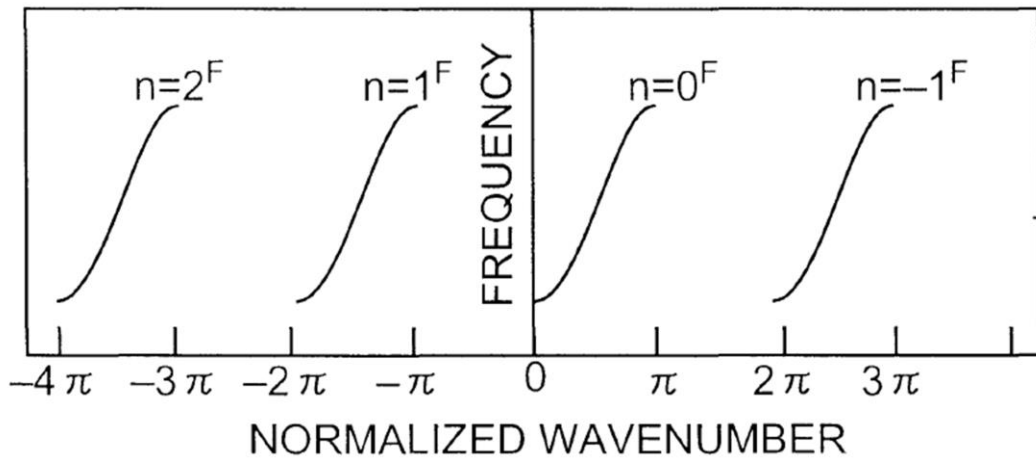


Fig. 2.8. The dispersion diagram of spatial harmonics propagating in the $+z$ direction for an infinitely long hypothetical SWS.

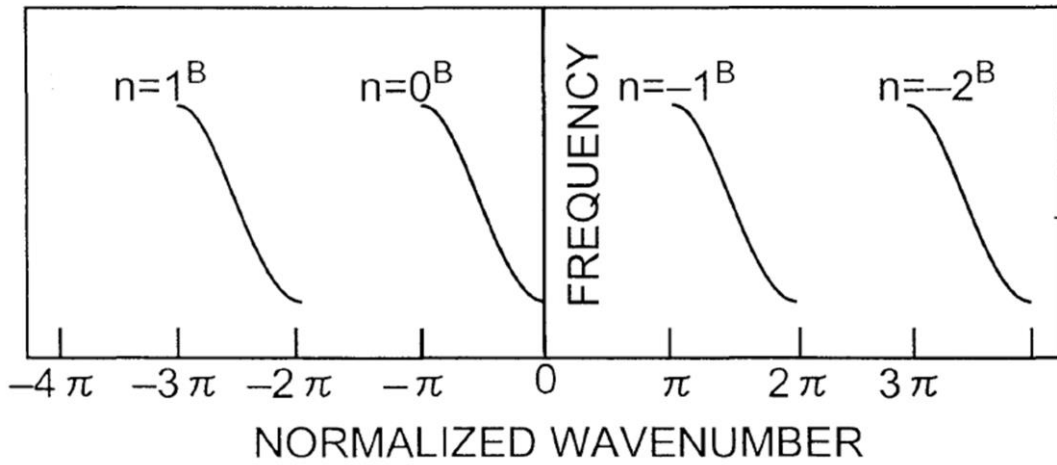


Fig. 2.9. The dispersion diagram of spatial harmonics propagating in the $-z$ direction for an infinitely long hypothetical SWS.

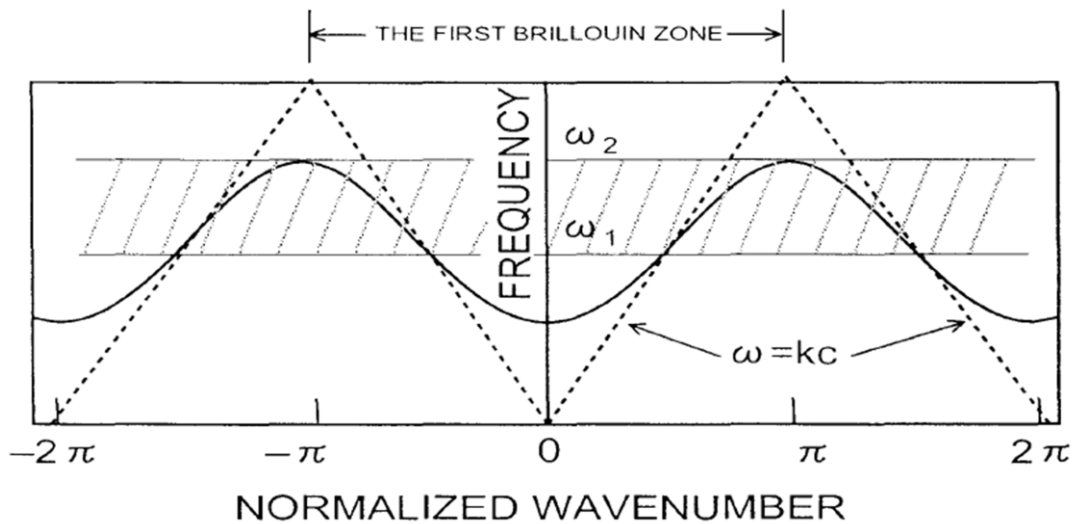


Fig. 2.10. The complete dispersion diagram for the fundamental mode of an infinite length SWS constructed by superimposing Fig. 2.8 and Fig. 2.9

2.3.2 Dispersion relationship of the G-band BWO

Fig. 2.11 shows dispersion curves of the fundamental axisymmetric transverse magnetic (TM_{01}) mode with the parameters in Table 2.1. The TM_{01} mode in the slow-wave region has a slower phase velocity than the velocity of light and becomes a surface wave near the upper cut off frequency at the π point ($k_z z_0 = \pi$). The dispersion curves in Fig. 2.11 are real number curves because the beam current is assumed to be zero. For a nonzero beam current, the beam interacts with the TM_{01} mode and the dispersion curves have imaginary parts corresponding to the

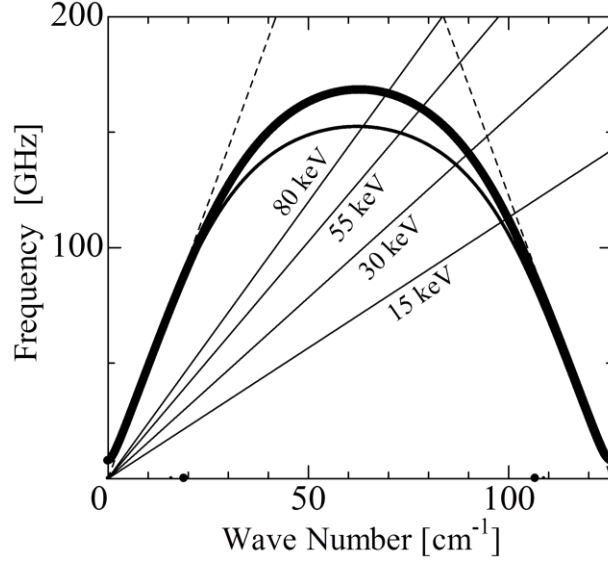


Fig. 2.11. Dispersion curves of surface wave for G-band corrugated hollow waveguide in Fig. 2.2 with parameters in Table 2.1. Thick and thin solid curves represent the designed and fabricated corrugations, respectively. Dotted lines are light lines. The results for a beam energy of 15 keV, 30 keV, 55keV, and 80 keV are also plotted. (From Ref. 61)

growth rate of the TM_{01} mode. The beam interaction becomes stronger upon increasing the beam energy, because the beam power increases and the group velocity of the TM_{01} mode decreases approaching the π point.

2.3.3 Dispersion relationship of the G-band CSW-resonator

Dispersion curves of the CSW are obtained by a numerical method based on a modal expansion of the electromagnetic field for corrugated feed-horns [47]. This method is successfully applied to CSWs on rectangularly corrugated cylinders [31], [48]. Here, we briefly summarize the mathematical formulation following that of Ref. 31. Outside of the corrugation, the fields are expanded in a spatial harmonic series in accordance with Floquet's theorem,

$$\begin{aligned}
 E_z^I &= \sum_{p=-\infty}^{\infty} A_p K_m(x_p r) \exp[i(k_z z + m\theta - \omega t)] \\
 B_z^I &= \sum_{p=-\infty}^{\infty} \frac{i}{c} B_p K_m(x_p r) \exp[i(k_z z + m\theta - \omega t)]
 \end{aligned} \tag{2.5}$$

Here, I_m and K_m are the first- and second-kind modified Bessel functions of m th-order,

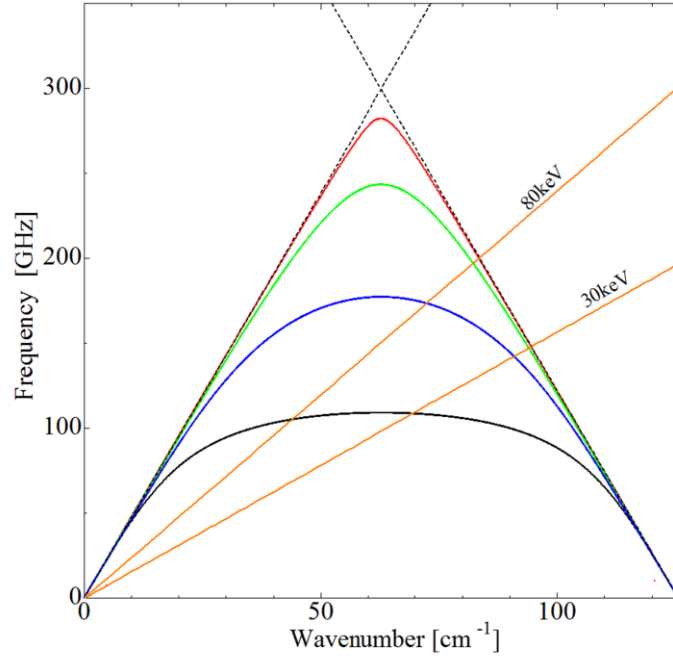


Fig. 2.12. Dispersion curves of the fundamental axisymmetric CSWs with the parameters $R_0 = 12.6$ mm, $d = 0.3$ mm, $z_0 = 0.5$ mm. Values of h are 0.035, 0.069, 0.135, and 0.27 mm, from the top. Dotted lines represent light lines. The results for beam energy of 30 keV and 80 keV are also plotted. (From Ref. 62)

respectively. Also $k_p = k_z + pk_0$, p is Floquet's harmonic number and

$$k_p^2 = k_z^2 - \frac{\omega^2}{c^2} \quad (2.6)$$

The constants A_p and B_p are coefficients of electromagnetic fields. The other field components can be derived from E_z and B_z . Inside the rectangular corrugation, electromagnetic waves may be expressed as a sum of standing waves which satisfy the boundary conditions at the corrugation walls. Boundary conditions between the two regions correlate Floquet's harmonics given by (2.5) and the standing waves inside the corrugation. This relationship may be formally expressed in terms of A_p and B_p as

$$\begin{bmatrix} \mathbf{C}^{(11)} \cdot \mathbf{A} + \mathbf{C}^{(12)} \cdot \mathbf{B} \\ \mathbf{C}^{(21)} \cdot \mathbf{A} + \mathbf{C}^{(22)} \cdot \mathbf{B} \end{bmatrix} = \begin{bmatrix} \mathbf{C}^{(11)} & \mathbf{C}^{(12)} \\ \mathbf{C}^{(21)} & \mathbf{C}^{(22)} \end{bmatrix} \cdot \begin{bmatrix} \mathbf{A} \\ \mathbf{B} \end{bmatrix} = \mathbf{0} \quad (2.7)$$

Here, \mathbf{A} and \mathbf{B} are column vectors with the elements A_p and B_p , respectively, and $C^{(ij)}$ with $1 \leq i, j \leq 2$ are matrixes of infinite rank. The dispersion characteristics are given by the condition that (2.7) has nontrivial solutions, that is,

$$\det \begin{bmatrix} C^{(11)} & C^{(12)} \\ C^{(21)} & C^{(22)} \end{bmatrix} = 0 \quad (2.8)$$

Numerical calculations in this paper, seven Floquet's harmonics with $-3 \leq p \leq 3$ and five standing waves from the lowest one are considered to assure the numerical convergence. For axisymmetric TM, $\mathbf{B} = 0$ and (2.8) becomes $\det[C^{(11)}] = 0$, which is simplified to the dispersion relation (2.7) in Ref. 48 when only the lowest standing wave is considered inside the corrugation.

Figure 2.12 shows the dispersion curves of the fundamental axisymmetric CSWs with the parameters $R_0 = 12.6$ mm, $d = 0.3$ mm, $z_0 = 0.5$ mm, and h varying from 0.035 mm to 0.27 mm. According to the Floquet's theorem, the dispersion curves are periodic in wavenumber space (k_z -space) with a period of $k_0 = 125.6$ cm⁻¹. In Fig. 2.12, one period from 0 to k_0 is shown on the basis of the periodic-zone scheme. The CSW curves are in the slow-wave region of the isosceles

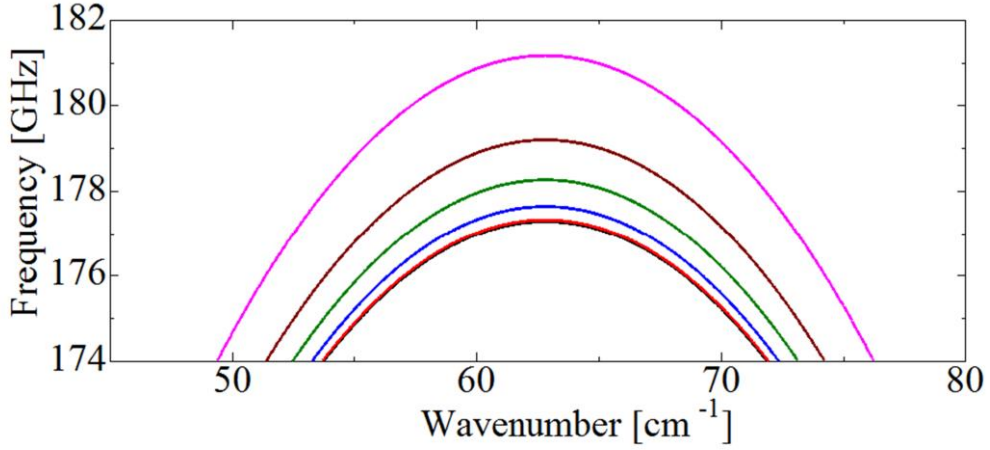


Fig. 2.13. Dispersion curves of axisymmetric and non-axisymmetric CSWs near the π point with the parameters $R_0 = 12.6$ mm, $d = 0.3$ mm, $z_0 = 0.5$ mm, and $h = 0.135$ mm. Values of azimuthal mode number m are 0, 1, 3, 5, 7 and 10, from the bottom. Two curves with $m = 0$ and 1 overlap and form the lowest curve. (From Ref. 62)

triangle formed by $\omega = k_z c$, $\omega = -(k_z - k_0)c$ and $\omega = 0$, in which the wave phase velocity is less than the velocity of light. The CSWs have an upper cut off frequency at the π point ($k_z z_0 = \pi$). The CSWs near the π point are located apart from the light line and are localized close to the corrugation surface. They are a bounded surface wave and form CSW-resonator [33].

There are non-axisymmetric CSWs in addition to the axisymmetric CSW and they exist very close to each other. Figure 2.13 shows the dispersion curves of CSW having azimuthal mode number m from zero to 10. The lowest curve is composed of two curves with $m = 0$ and 1. And curves up to about $m = 6$ coincide within 1 %. Our CSW-resonator is oversized with $D/\lambda \gg 1$ and a multimode system. The multimode nature is in contrast to the non-oversized case, for which the axisymmetric and non-axisymmetric CSWs exist apart from each other [48].

Compared with the other parameters, the corrugation amplitude h has a significant impact on the frequency and the upper cut off frequency at the π point increases by decreasing h as shown in Fig. 2.12. Another important factor to be considered in realistic devices is the finiteness of the CSW-resonator length L . In our experiment, L takes of values of $20z_0$, $40z_0$ and $80z_0$.

2.4 Summary and Discussion

The G-band slow wave structures have been analyzed. The dispersion relation, Cherenkov interaction and Floquet harmonics for the fundamental and higher axial modes have been analyzed in detail. And in next chapter, the electron beam and cathode used in this work will be discussed.

3 ELECTRON BEAM AND CATHODE

3.1 Electron Beam

Stream of electrons generated by heat, bombardment of charged atoms or particles, or strong electric fields. Electrons may be collimated by holes and slits, and, because they are electrically charged, they may be deflected, focused, and energized by electric and magnetic fields. Electron beams are used chiefly in research, technology, and medical therapy to produce X-rays and images on television screens, oscilloscopes, and electron microscopes.

Electron beams have been developed for microwave sources, in the gigahertz (GHz) and terahertz (THz) regions. Such microwave sources are in widespread use in nondestructive inspection and communications systems. Slow-wave devices such as BWOs and TWTs can be driven by an axially injected electron beam and have been extensively studied for many decades as a family of HPM sources. For such microwave sources, it is essential to use reliable cathodes producing a high-current electron beam with a uniformly distributed cross-sectional shape.

3.2 Electron Beam Diode

The annular electron beam is generated by a magnetically insulated beam diode that consists of a hollow anode and a disk copper cold cathode. The anode-cathode (A-K) configuration of the beam diode is shown in Fig. 3.1. The distance between the anode and the cathode (A-K gap) can be varied from 0 to 25 mm by using a linear introducer. In our experiment, the A-K gap is set at 10 mm.

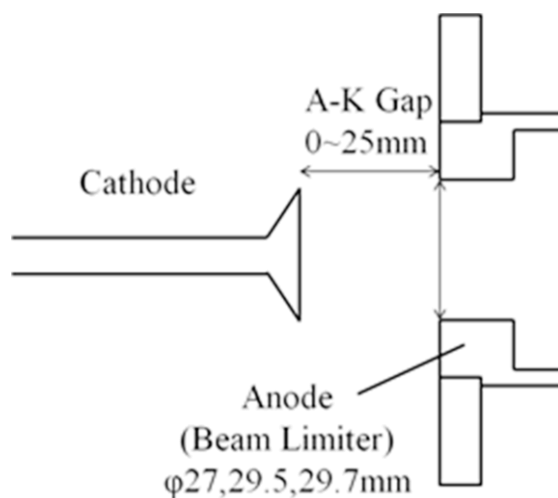


Fig. 3.1. Electron beam diode

3.3 Cathode

Cold cathodes are very simple and useful especially for pulsed high-power operation [49]. They can produce fairly uniform electron beams, whose uniformity can be further improved with the help of dielectrics in the relativistic region higher than hundreds of kilovolts. For example, the cathode surface is coated with a mixture of fine graphite powder and epoxy to increase the beam uniformity. However, the generation of a uniform electron beam becomes increasingly difficult as the cathode voltage becomes lower in a weakly relativistic region of less than 100 kV. At such low beam voltages, the use of dielectric fibers such as velvet and carbon fibers has been indispensable. The velvet cathode is typically used in high-power devices. An attractive alternative to the cold cathode is a disk-type cathode, which can realize stable relativistic electron beams by reducing unwanted plasma generation at the cathode surface [50].

The typical cold cathode with and without velvet used in this work are shown in Fig. 3.2(a) and Fig. 3.2(b) and are made of oxygen-free copper. In the velvet cathode, plasma is formed by the flashover of the dielectric velvet fiber's surface and the electron emission areas cover the velvet belts. Velvet or surface roughness on the emission surface is required for uniform electron emission. They are both useful in rather high-voltage region above about 60 kV to 100 kV. In a low-voltage region below about 60 kV to 10 kV, velvet is more suitable. The thickness of the annular beams is typically 2-3 mm and the diameter of the electron beam can be changed by changing the diameter of the cathode. Annular beams with nearly the same diameter as the cathode diameter are obtained in the weakly relativistic region.

3.4 Burn Pattern of Electron Beam

The electron beam shape along the transport section is examined by observing the burn pattern in thermal-sensitive paper placed in the propagating beam. The electron beam current on the beam collector located at 228 mm from the hollow anode is measured using a current monitor. The experimental setup for burn pattern experiment is schematically shown in Fig. 3.3. To prevent the erosion of the corrugation by the high-energy beam, we set a beam limiter at the entrance of the waveguide. We can also obtain an electron beam with a different diameter by changing the beam limiter. The beam shape is observed from burn patterns in thermally sensitive paper as shown in Fig. 3.4. The patterns are taken by a single shot with a beam energy of about 80 keV. A disk cathode with a diameter of 29 mm is used and uniformly distributed annular beams are obtained as shown in Fig. 3.4. In Fig. 3.4, two beam limiters with diameters of 29.5 mm and 29.7 mm are used, and the difference between the two diameters is 0.2 mm. Since such a small difference in the outer diameter cannot be clearly shown by the burn patterns, the two uniformly distributed patterns in Fig. 3.4 appear to be almost the same. The burn

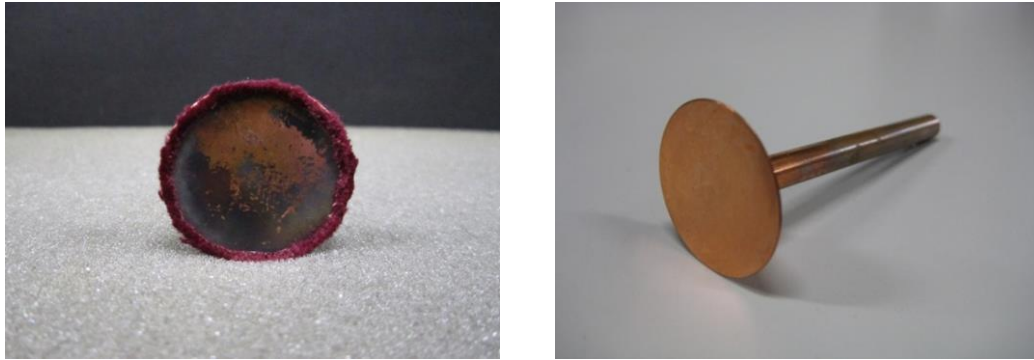


Fig. 3.2. Photograph for a disk cold cathode of diameter 27 mm. Left: with velvet. Right: without velvet.

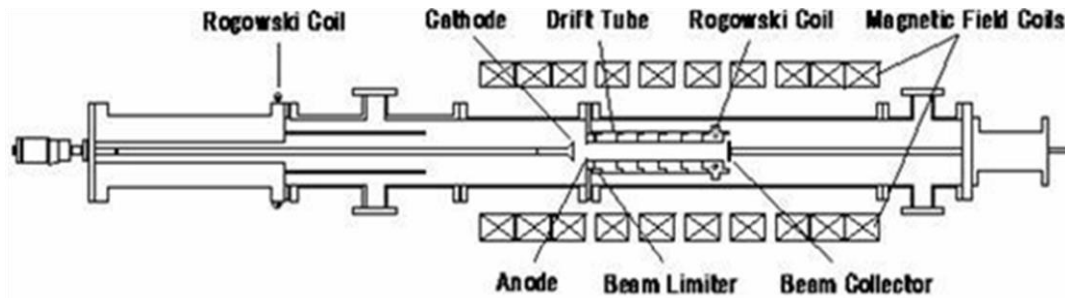


Fig. 3.3. Schematic diagram of the experimental setup for burn pattern experiment

patterns with different beam energy have investigated in detail as shown in Fig. 3.5. In this figure a disk cathode with a diameter of 27 mm is used and uniformly distributed annular beams are obtained in a fairly broad beam energy region from about 20 keV to 100 keV. Our experimental results show that the size of the sites needs to be on the order of micrometers and distributed along the emission edges of the cathode to form a uniform electron emission surface.

3.5 Beam Generation

An electron beam diode and a beam collector are installed in a stain less steel vacuum vessel. The vacuum system consists of a turbo molecular pump backed by a rotary pump. The background residual gas pressure is kept under 1×10^{-5} Torr. A ten-stage 1-kJ Marx generator is used as the high-voltage source. In the experiments, output voltages of the pulse forming line (PFL) ranging from about 30 to 100 kV are applied to the cathode. The magnetic field for beam generation is provided by ten solenoid magnetic field coils. The position of each coil is adjusted so that the beam diode, beam transport section, and beam collector lie in a uniform region of 0.82 T.

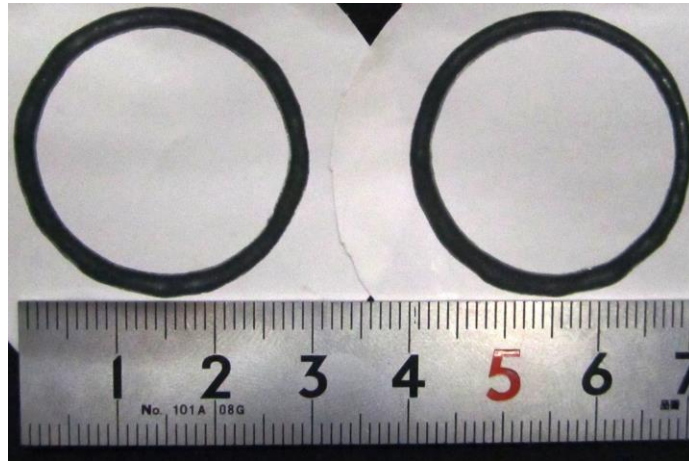


Fig. 3.4. Burn patterns of electron beam for a disk cathode of diameter 29 mm. The diameters of the beam limiter are 29.5 mm (left) and 29.7 mm (right). (From Ref. 61)



Fig. 3.5. Burn patterns of electron beam for a disk cathode of diameter 27 mm. Left: the beam energy is about 30 keV (with velvet). Right: the beam energy is about 80 keV (without velvet). (From Ref. 62)

The diode voltages versus beam current characteristics are important for stable electron beam generation. The time evolutions of the diode voltage and beam current for a successful case of uniform beam generation are shown in Fig. 3.6. In the figure, the peak current is about 500 A at about 50 kV, and the current exhibits peaks at a lower voltage. The current rise time is long, because plasma generations are slow owing to the insufficient roughness of the emission surface.

3.6 Principle of Electron Emission

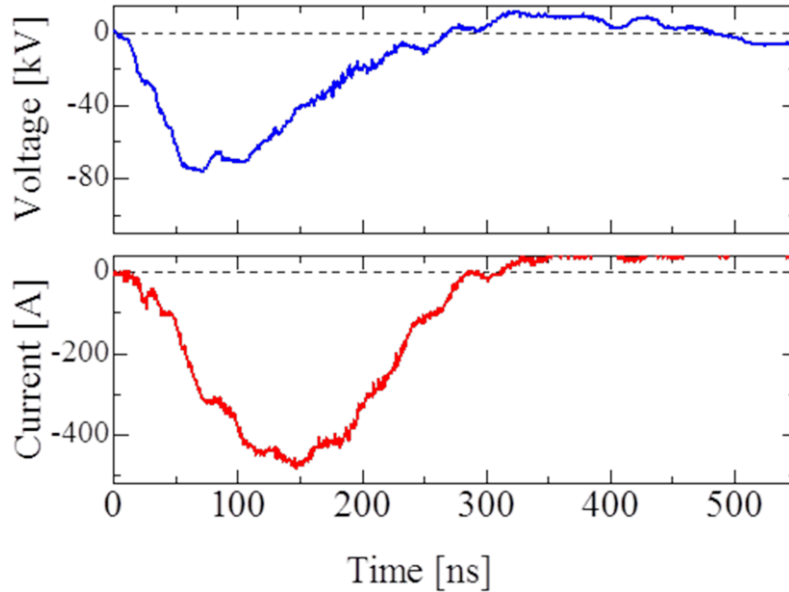


Fig. 3.6. Time evolutions of diode voltage and beam current for a disk cathode.

3.6.1 Explosive electron emission

As the electron emission mechanism of a cold cathode, a single kind of emission i.e. explosive electron emission (EEE) can be listed for example. For EEE, the electrons are emitted from high-density plasma produced on the surface and the axis of the cathode by adding a strong electric field on the cathode surface. The main point of this mechanism is the plasma generation from the cathode, and EEE can be divided into the following two types by the plasma generation process.

- Field-enhancement EEE
- Surface-flashover EEE

3.6.2 Field-enhancement EEE

Field-enhancement EEE occurs mainly in the metal surface. The disk-type cathode used in this work can also be explained by the cathode plasma generation process. It looks like the cathode surface is smooth, but there are a large number of small protrusions (height less than 10^{-4} cm, the radius of the root less than 10^{-5} cm). First, when an electric field is applied between the electrodes the electric field is concentrated on the tip of the protrusions. The electric field at this time is 10^7 V/m or more. Thus, electron field emission occurs from the tip of the protrusions. Since the electron current focus on the protrusions, resistance overheating (Joule heat) is remarkable. By this heating, the protrusions undergo metal evaporation vaporization. The plasma is generated in the ionization to the cathode surface. The plasma at this time is several thousand K at least.

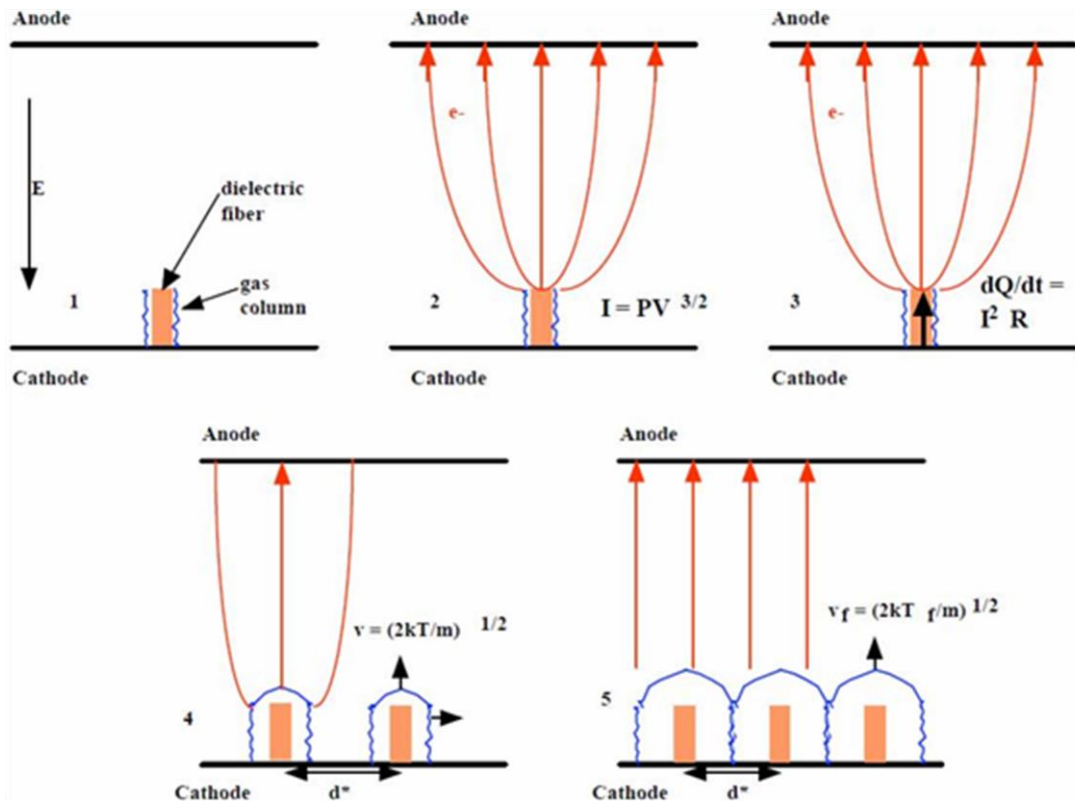


Fig. 3.7. The electron emission model based on velvet proposed by R. B. Miller. (From Ref. 63)

3.6.3 Surface-flashover EEE

The dielectric fibers (velvet) are pasted to the tip of the cathode, where the electron beam is generated by electric field emission. For plasma generation, velvet has a low electric field threshold and the uniform electron emission can be obtained. The electron emission mechanism using velvet based on the field emission model proposed by R. B. Miller can be described in five steps as shown in Fig. 3.7.

- (1) When an electric field along the velvet exceeds a threshold, surface flashover occurs and dense plasma gas is generated at a low temperature.
- (2) At this time the electrons flow is pulled out by the electric field on the surface of the velvet, the limited space charge current is pulled out from the plasms gas.
- (3) Plasma gas is heated by resistive heating caused by the current through the gas.
- (4) Gas pillars spreads at a rate that is proportional to the square root of the gas temperature.
- (5) The plasms continue to spread, and the electrons flow occurs in avalanche.

3.7 Summary and Discussion

For high-power microwave sources, beam sources are key technologies. In the relativistic

region, high-current electron beams are obtained using cold cathodes based on explosive uniform electron emission. However, it is very difficult to realize a uniform electron beam using cold cathodes in weakly relativistic regions. In this chapter, electron beam generation in a weakly relativistic region of less than 100 kV was investigated utilizing disk cold cathodes made of copper. The electron emission surfaces are located on the sharp edges of the cathodes. The electron beam shape along the transport section is examined by observing the burn pattern in thermal-sensitive paper placed in the propagating beam. The uniform electron beams generated in this chapter are used in high-power microwave operation in our work.

4 EXPERIMENTAL STUDIES ON G-BAND BACKWARD WAVE OSCILLATOR AND CYLINDRICAL SURFACE WAVE RESONATOR

4.1 Experimental Setup

The experimental setup is shown in Fig. 4.1. Photographs for the different components are shown in Fig. 4.2. Brief descriptions for some of the components of Fig. 4.2 are given below.

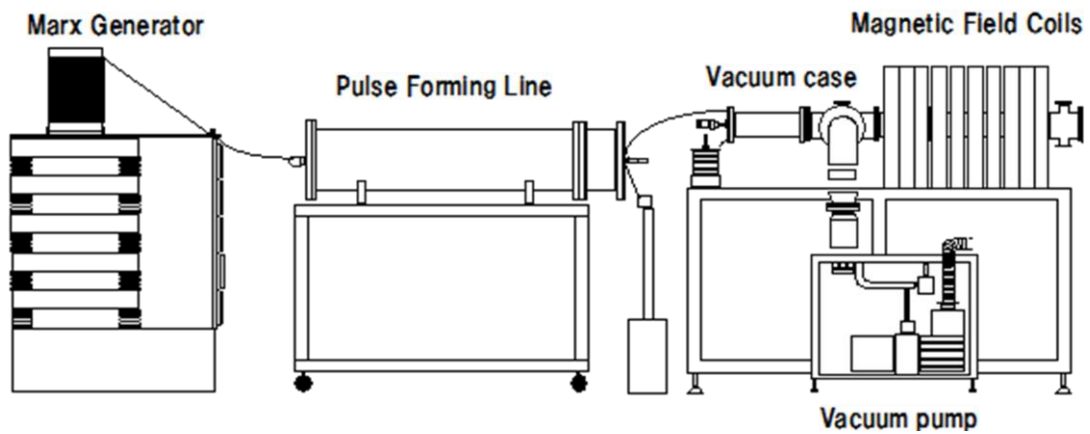


Fig. 4.1. Schematic diagram of the experimental setup.



Fig. 4.2. Schematic diagram of the experimental setup.

4.1.1 Marx generator

Marx generator (IG-H200) has been used as a high voltage source to generate the electron beam in our experiments. A photograph of the Marx generator is shown in Fig. 4.3. As can be seen from Fig. 4.3, ten 0.5 μF capacitors are charged via resistors connected in parallel. By closing the gap of the mechanical electromagnet driving, the ten charged capacitors are switched in series, and a high voltage has been generated.

First, Marx generator is charged to a desired voltage then discharge command is sent by the sequence controller T_d s after triggering the magnetic power supply. The time delay is needed to reach the B_0 pulse at the flattop region.

4.1.2 Pulse forming line

Pulsed forming line (PFL) is a distributed constant circuit for pulse forming. High density electric power is formed by compression of the impulse voltage generated from the Marx generator, i.e. PFL is a pulse power generator. The obtained pulse power is applied to the diode, the electron beam can be generated efficiently with a large current and high voltage. The appearance of the PFL used in this work is shown in Fig. 4.4.

When the PFL capacity is equal to the MG capacity the energy transfer efficiency is 100%. We have used a stainless steel tube as PFL material. The size and withstand voltage are limited, and an abnormal discharge does not occur, which are suitable for the operations. The inner diameter of the outer conductor and the outer diameter of the inner conductor are 261.4 mm and 89.2 mm, respectively.

As inductor insulating oil and water are used in PFL. Pure water with high dielectric strength



Fig. 4.3. Photograph of the Marx generator.

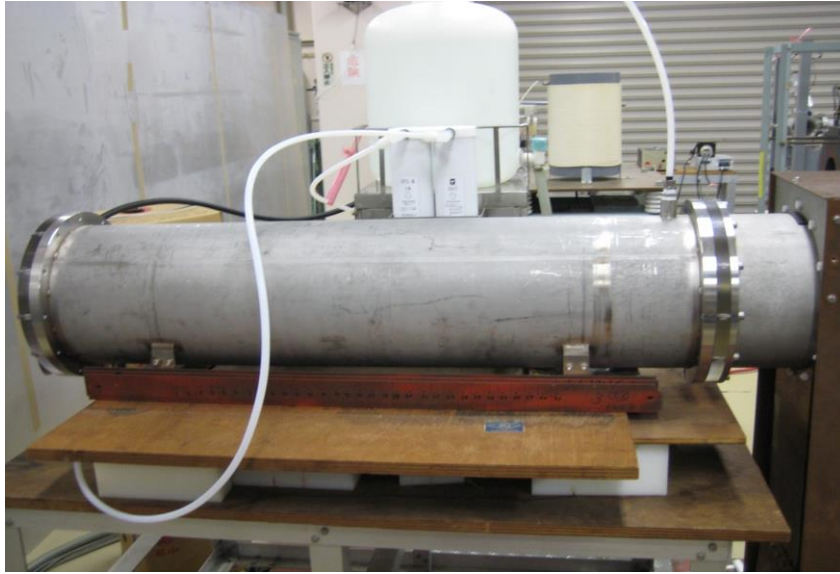


Fig. 4.4. Photograph of the Pulsed forming line (PFL).

and higher dielectric constant is possible to constitute a compact line in the high voltage region with a low characteristic impedance. In order to maintain the electrical characteristics of the pure water as much as possible, it is necessary to make the water circulated by a pump through the ion exchange resin filtration.

Here, the radius of the outer diameter of the inner conductor is a , the radius of the inner diameter of the outer conductor is b and we consider the length in fact is 1 m. The formula for calculating the distribution capacity C [F/m] of cylindrical coaxial line, as well as the direct cylindrical capacitor in the electromagnetism region is shown as below:

$$C = \frac{2\pi\epsilon}{\log(b/a)} \quad (4.1)$$

Formula for calculating the inductance distribution L [H/m] is

$$L = \frac{\mu}{2\pi} \log \frac{b}{a} . \quad (4.2)$$

The characteristic impedance Z_c is

$$Z_c = \sqrt{\frac{L}{C}} = \frac{1}{2\pi} \sqrt{\frac{\mu}{\epsilon}} \log \frac{b}{a} . \quad (4.3)$$

Specific Dielectric Constant ϵ_s	81
Specific Magnetic Permeability μ_s	1
Specific Resistance ρ	2.5×10^{-5} [Ω/m]
Withstand Voltage (40 μ sec)	200 [kV/cm]

Table 4.1. Characteristics of the pure water.

Distribution Capacity C	4.14 [nF/m]
Distribution Inductance L	215 [nH/m]
Characteristic Impedance Z_C	7.21 [Ω]

Table 4.2. Characteristics of Pulsed forming line (PFL).

Here, the dielectric constant ϵ and the magnetic permeability μ of the internal inductor and the characteristics of the pure water and PFL are shown in Table. 4.1 and Table. 4.2, respectively.

4.1.3 Guiding magnetic field

The guiding magnetic field, B_0 , is provided by ten solenoid coils designed for pulsed and continuous operations. Coils are connected to a variable power supply unit capable of supplying



Fig. 4.5. Left: Magnetic field power supply controller, Right: DC current source.



Fig. 4.6. Photograph of the Magnetic field coils.

Output Current Setting	Current Flowing in the Magnetic Field Coils [A]	Axial Magnetic Field B_z [T]
1	36.6	0.0789
2	86.7	0.177
3	138.4	0.276
4	188.6	0.375
5	242.7	0.473
6	291.6	0.572
7	345.2	0.67
8	398.6	0.769
9	449.6	0.868
10	501.4	0.986

Table. 4.3. Current flowing in the magnetic field coils and guide magnetic field.

current up to 500 A which corresponds to $B_{max} = 0.986$ T. The device for DC current flows through the coils is shown in Fig. 4.5. In Fig. 4.5, on the left hand is magnetic field power supply controller and on the right hand is the DC current source. The rated maximum output power for source is 500 A so we must use it very carefully in our experiments. Figure 4.6 shows the photograph of the coils. The spatial variations of B_0 measured by a Gauss meter over the region extending from the cathode to the output window. The coil spacing are optimized so that the beam diode and the SWS lie on the maximum B_0 region. The tapering of the magnetic field

which begins near the SWS exit facilitates the beam dumping. The Marx generator and the coil power supply are controlled by the sequence controller. As described earlier, after charging the Marx generator to a desired voltage its output switch is triggered 1800 ms after triggering the magnetic coil power supply. Hence, high voltage pulse is applied to the cathode when B_0 pulse reached at the flattop region. Moreover, the relation of the current flowing in the coils and the magnetic field is shown in Table. 4.3.

4.1.4 Vacuum device

In order to realize stable electron emission, it is necessary to set the vacuum device for a high vacuum state. In our laboratory we have used an oil rotary pump and a turbo-molecular pump as the vacuum gauge. The appearance of the vacuum device is shown in Fig. 4.7. Vacuum vessel is a cylindrical container with full length 900 mm and inner diameter 160 mm. The high voltage introduction portion, the electron beam diode, the slow wave waveguide, and Rogowski coil are set inside. In order to avoid the leak which occurs at the junction of the cylindrical container and the flange, gasket and O ring are used.

4.1.5 Rogowski coil

The beam current is monitored by a Rogowski coil designed for monitoring nanosecond order current pulse. The coil is located at the entrance of the SWS which encircled the electron beam completely. The Rogowski coil is also calibrated by using the Marx generator with 200 Ω load resistance. Fig. 4.8 shows a structural diagram of a Rogowski coil that used in the experiments.



Fig. 4.7. Photograph of the vacuum device.

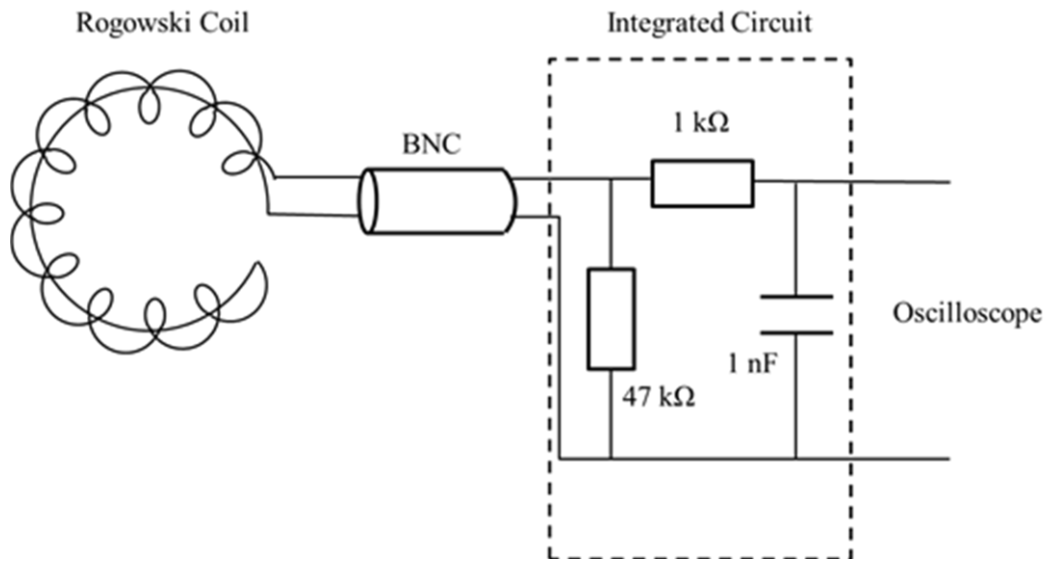


Fig. 4.8. Structural diagram of the Rogowski coil

4.1.6 Microwave detection system

The microwaves are picked up by rectangular horn antennas connected to waveguides of the D-, G-, and H-bands in our experiments, which are the Electronic Industries Alliance (EIA) standard rectangular waveguides with cut off frequencies of 91, 116, and 173 GHz, respectively [51]. The recommended frequency range, the cutoff frequency, and the EIA designation for D-, G-, and H-band are shown in Table. 4.4.

4.2 Frequency Measuring Experiment

4.2.1 G-band BWO

The operation frequency of the G-band BWO is examined by using rectangular waveguides with various cut off frequencies. The estimated frequency is in the range of 151-157 GHz with a

Band	Recommended Frequency Range(GHz)	TE01 Cutoff Frequency (GHz)	EIA Designation
D	110-170	90.854	WR-6
G	140-220	115.75	WR-5
H	220-325	173.28	WR-3

Table. 4.4. Waveguide standard

beam voltage of 60-70 kV.

4.2.2 G-band CSW-resonator

To obtain the real operation frequencies, we prepare high-pass filters with cut off frequency of about 157, 166, 175, 182, 200, and 250 GHz. The estimated operation frequency for A (B)-type corrugation is in the range of 166-173 GHz (182-200 GHz) which is consistent with the theoretical predictions in Fig. 2.12.

4.3 Microwave Oscillation Experiment

4.3.1 G-band BWO

The experimental setup using the corrugated hollow waveguide as G-band BWO is schematically shown in Fig. 4.9. Fig. 4.10 shows typical waveforms of microwave signals for G-band BWO with length $L = 20z_0$, $40z_0$, and $80z_0$. The microwave signal in Fig. 4.10 is detected by the D-band (110-170 GHz) rectangular horn antenna at a position 600 mm away from the output window, and 10 dB, 20 dB attenuation are used. We evaluated the detected powers for $L = 20z_0$, $40z_0$, and $80z_0$ using the voltage signals of the microwave. In the experiment, the voltage and current change with time, as shown in Fig. 4.10, and their values at the time of the microwave peak are used.

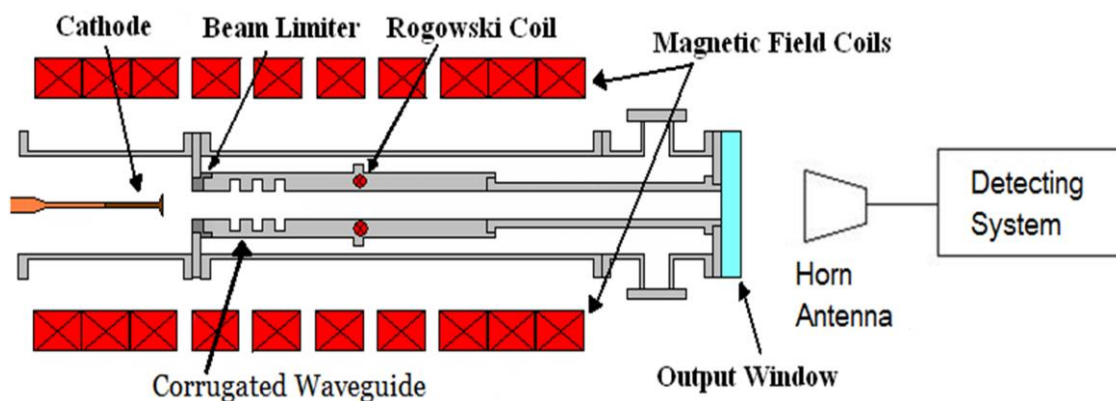


Fig. 4.9. Schematic diagram of the experimental setup for G-band BWO

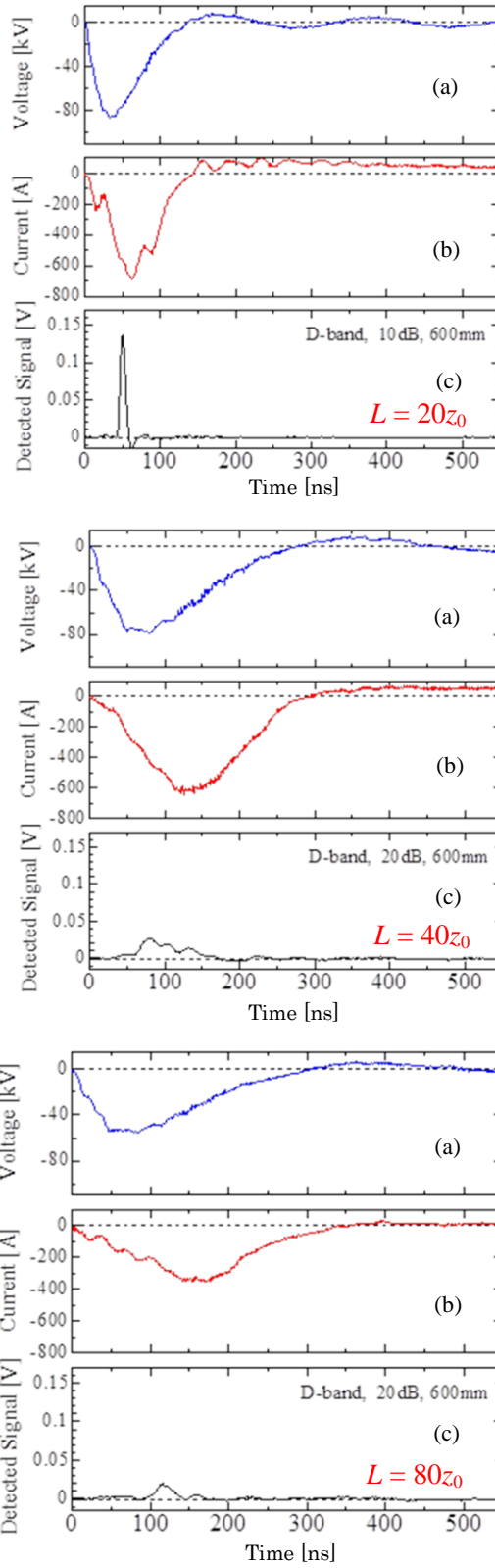


Fig. 4.10. Typical waveforms of measured signals in G-band BWO with 20, 40, and 80 periods from top: (a) beam voltage, (b) beam current, (c) microwave signal.

4.3.2 G-band CSW-resonator

The experimental setup using the corrugated cylinder is schematically shown in Fig. 4.11. Fig. 4.12 (Fig. 4.13) shows waveforms of measured signals when using an A (B)-type corrugated cylinder in Table 2.2 with SWS length $L = 80z_0$. The microwave signals are detected by the D-band rectangular horn antenna at a position 600 mm away from the output window and 10-dB attenuation is used. The EIA D-band detecting system has a cut off frequency of 91 GHz and can detect radiations with the frequencies at the crossing points between the CSW curves and the beam lines in Fig. 2.12.

4.4 Microwave Power versus SWS Length

4.4.1 G-band BWO

We evaluated the detected powers for $L = 20z_0$, $40z_0$, and $80z_0$ using the voltage signals of the microwave as shown in Fig. 4.14. The radiation power is estimated using the D-band (110-170 GHz) system since the voltages of the D-band detector are calibrated to absolute powers by using a Gunn oscillator at 100 GHz. In Ref. 24, an oversized G-band BWO with length $L = 80z_0$ was examined. The maximum detected power level was evaluated to be on the order of W by considering the 10 or 20 dB attenuation provided by the detecting system. By integrating the detected powers over the broad pattern, the total radiation power in terms of TM-like mode is roughly estimated to be on the order of some kW. In this work, it is demonstrated that the BWO radiation with $L = 40z_0$ is more intense than that with $L = 80z_0$ as shown in Fig. 4.14 and then the maximum radiation power of the G-band BWO increases and is estimated to be above 10

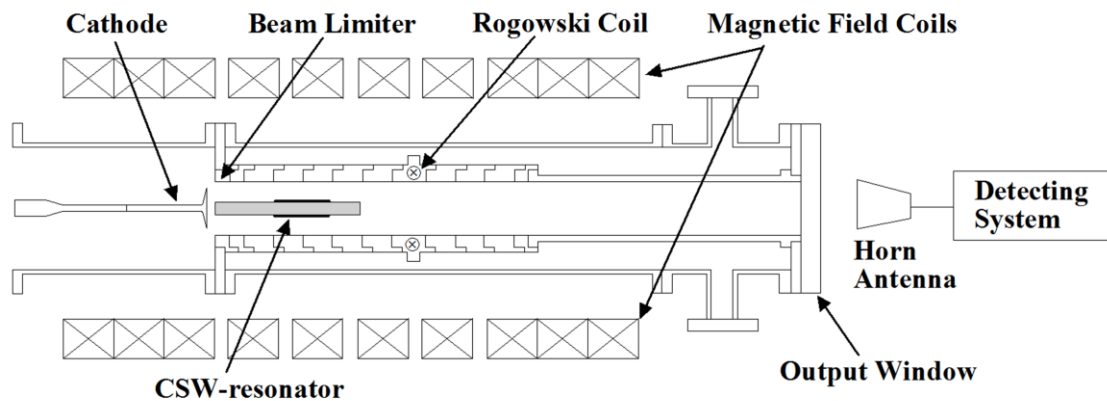


Fig. 4.11. Schematic diagram of the experimental setup for G-band CSW-resonator

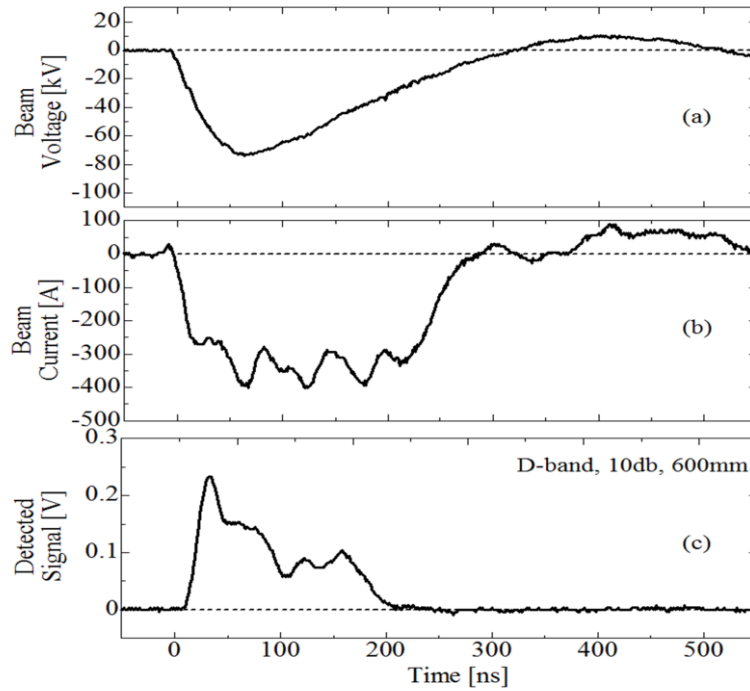


Fig. 4.12. Waveforms of measured signals for the A-type CSW-resonator: (a) beam voltage, (b) beam current, (c) microwave signal. The peak values of the beam voltage and current are about 80 kV and 400 A, respectively. (From Ref. 62)

kW.

4.4.2 G-band CSW-resonator

We evaluated the detected powers from the voltage signals of the D-band detecting system, which are calibrated to absolute powers by using a Gunn oscillator at 100 GHz. Fig. 4.15 (Fig. 4.16) shows the detected microwave power and beam current versus the beam voltage for A (B)-type CSW-resonator. In the experiment, the voltage and current change with time, as shown in Fig. 4.12 and Fig. 4.13, and their values at the time of the microwave peak are used. We find that the microwaves appear above a critical voltage, as shown in Fig. 4.15 and Fig. 4.16. In Fig. 4.15, the main challenge in the experiment was to achieve CSW-resonator operation over a wide range of beam voltage. For a particular cold cathode prepared, the variation in the beam voltage might be limited. By checking the beam uniformity like Fig. 3.5, we used the cathode with velvet which is both useful in low- and high-voltage region for $L = 40z_0$ or $80z_0$. And for $L = 20z_0$, the oscillations are just excited in high-voltage region so we choose the cathode without velvet. The closed plots and the open plots for $L = 40z_0$ and $80z_0$ in Fig. 4.15 had been obtained in different series of experiment. Unfortunately, we could not perform experiments with exactly

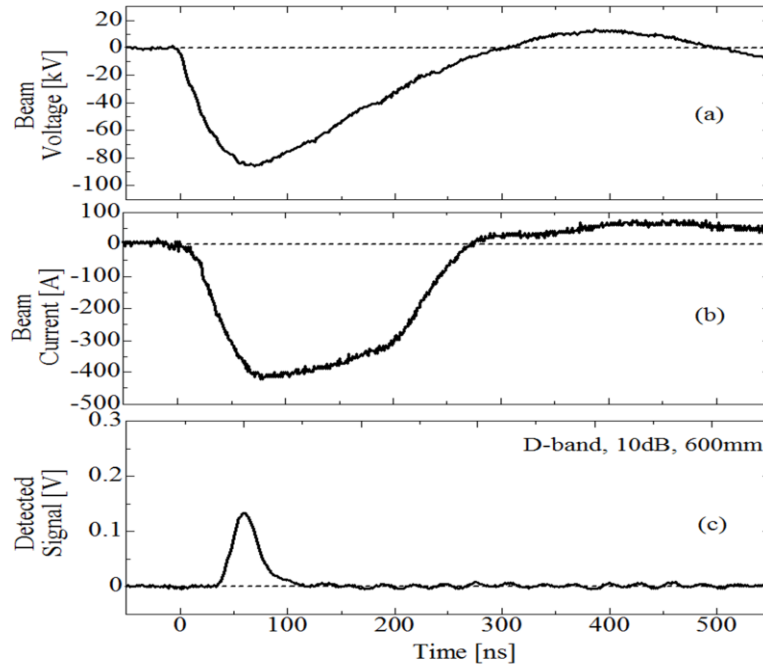


Fig. 4.13. Waveforms of measured signals for the B-type CSW-resonator: (a) beam voltage, (b) beam current, (c) microwave signal. The peak values of the beam voltage and current are about 90 kV and 430 A, respectively. (From Ref. 62)

the same angle with the same L among experimental series. However, for a fixed SWS the different angle from +10 degree to +5 degree makes virtually negligible influence on the output power as can be seen from the broad radiation pattern results. For $L = 80z_0$ in Fig. 4.15, the starting energy is about 26 keV. Above this, the output microwave can be identified clearly. The starting energy increases to about 42 keV for $L = 40z_0$, and to about 64 keV for $L = 20z_0$. We can find the oscillation starting energy increases with decreasing the SWS length L . Furthermore, with a fixed $L (= 80z_0)$, the starting energy increases by decreasing the corrugation amplitude h : from about 26 keV with $h = 0.135$ mm to about 70 keV with $h = 0.069$ mm. The oscillation for the B-type CSW-resonator with $L = 40z_0$ is not occur in Fig. 4.16 with the electron beam less than 100 keV. The starting energy for the A-type CSW-resonator is much lower than that for the B-type CSW-resonator. Hence, a range of beam energy for the oscillations of the A type CSW-resonator becomes wider than that of B-type CSW-resonator and the microwave pulse in Fig. 4.12 becomes longer than that in Fig. 4.13.

4.5 Radiation Pattern of The Output Microwaves

4.5.1 G-band BWO

The radiation patterns are obtained by moving a receiving horn antenna in an equatorial plane around a pivot at the center of output window. Horizontal (E_θ) and vertical (E_ϕ) components of the electric field are measured. The pattern of E_θ is shown Fig. 4.17. As a reference, a theoretical radiation curve of TM_{01} waveguide mode is shown. It is clear that a single TM_{01} mode cannot explain the radiation pattern. Higher order waveguide modes up to about TM_{10} are required to explain the radiation spreading beyond 30 degree. Excited surface waves in the SWS section go into the straight waveguide section before radiating from the output window as is shown in Fig. 4.17. On the boundary between the SWS and the straight waveguide, the excited surface wave couples to the straight waveguide modes including many higher order modes as well as the lowest TM mode. Pure TM (TE) modes have no E_ϕ (E_θ) component. The measured radiation patterns are broad and both TM and TE components are detected in the same level. This shows that slow-wave hybrid modes as well as the slow-wave TM_{01} mode may be radiated. The slow-wave hybrid modes are very close to the slow-wave TM_{01} mode and have almost the same dispersion characteristics in the beam interaction region as numerically shown in Ref. 52. The starting energy of the EH_{11} mode is almost the same as that of the TM_{01} mode and decreases by

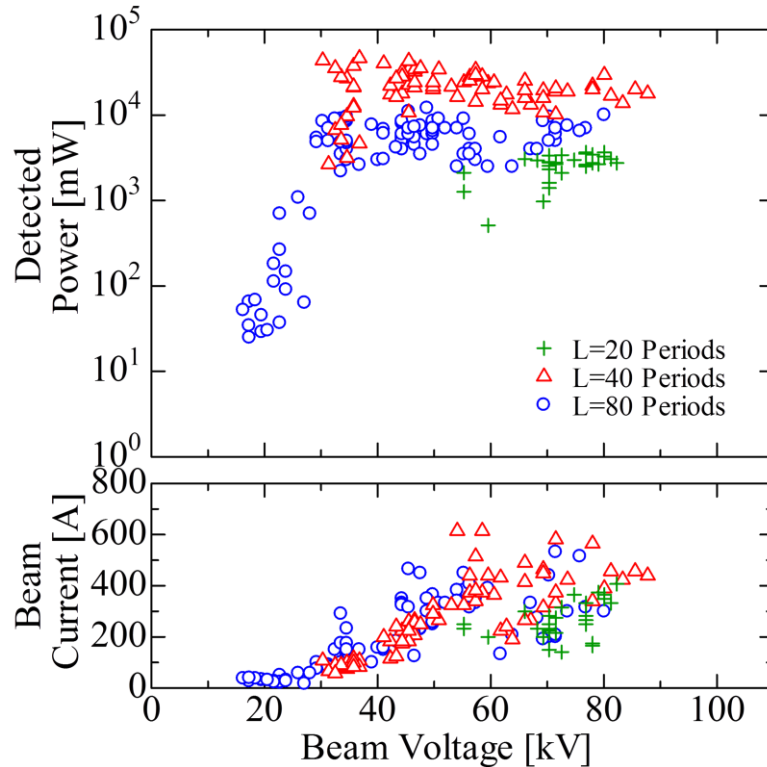


Fig. 4.14. Detected power and beam current versus beam voltage for G-band BWO with SWS length $L = 20z_0, 40z_0,$ and $80z_0$. (From Ref. 61)

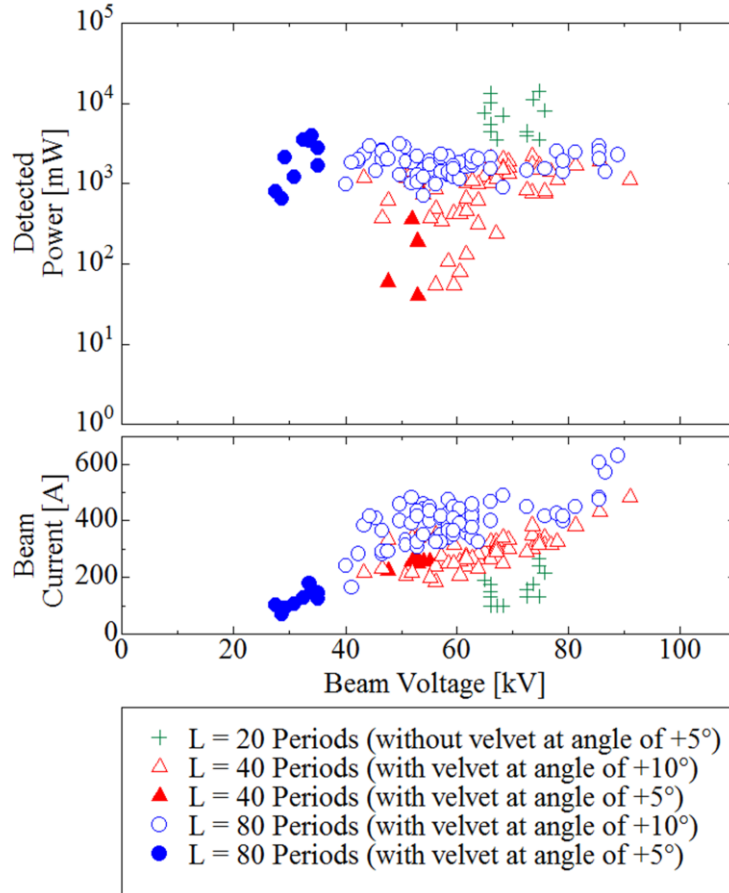


Fig. 4.15. Detected power and beam current versus beam voltage for the A-type G-band CSW-resonator with the length $L = 20z_0$, $40z_0$ and $80z_0$. (From Ref. 62)

increasing the azimuthal mode number. If the TM_{01} mode and the hybrid modes do not interact non-linearly, the starting condition can be discussed representatively based on the TM_{01} dispersion curve like oversized K-band BWO experiments in [13, 53], and this paper may properly demonstrate the oscillation-starting condition of our oversized G-band BWO.

We have studied weakly relativistic oversized BWOs in the K- and Q-bands. These BWOs are driven by an annular electron beam with energy less than 100 keV. The radiation powers are up to about 500 and 200 kW for the K- and Q-band BWOs, respectively [10]. The figure of merit Pf^2 of our weakly relativistic BWO is about 3×10^2 [MW · GHz²]. The oversized G-band BWO presented in this study realizes intense radiation on the order of 10 kW and has the same figure of merit as the lower-frequency BWOs in the K- and Q-bands. In Fig. 4.14, intense radiation can be observed in the voltage range from about 30 to 90 kV with a beam current from 100 to 600 A. The electronic efficiency is roughly estimated to be on the order of 0.01 to 0.1%. The interaction between the waveguide corrugations and the beams almost uses the outer tip of the annular

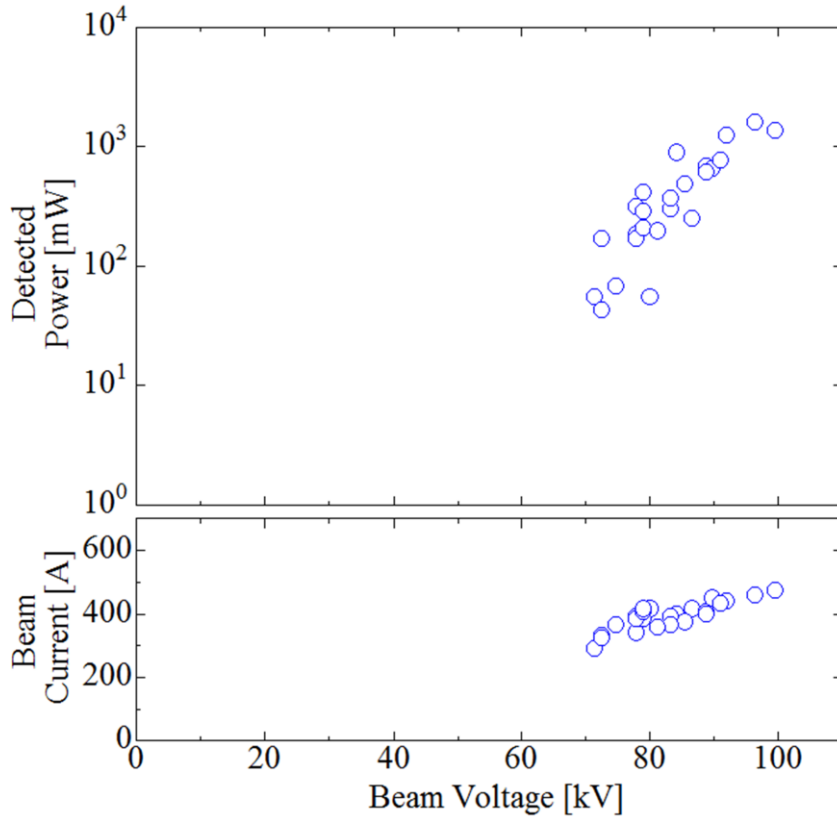


Fig. 4.16. Detected power and beam current versus beam voltage for the B-type G-band CSW-resonator with the length $L = 80z_0$. (From Ref. 62)

beams shown in Fig. 3.4. We consider that the measured electronic efficiency will increase upon removing the unused inner section of the annular beams.

4.5.2 G-band CSW-resonator

Radiation patterns are obtained by moving a receiving horn antenna in an equatorial plane around a pivot at the center of output window. Horizontal (E_θ) and vertical (E_ϕ) components of the electric field are measured and are plotted as a function of detecting angle in Fig. 4.18. Both E_θ and E_ϕ components are detected in the same level. The measured patterns are broad Gaussian-like beams with a maximum near the center. As a reference of a Gaussian beam, a theoretical radiation curve of TE_{11} mode is also shown in Fig. 4.18. It is clear that a single TE_{11} mode cannot explain the radiation pattern. Our CSW-resonator is an oversized multimode system, where many CSWs may be excited. The excited CSWs in the CSW-resonator go to the

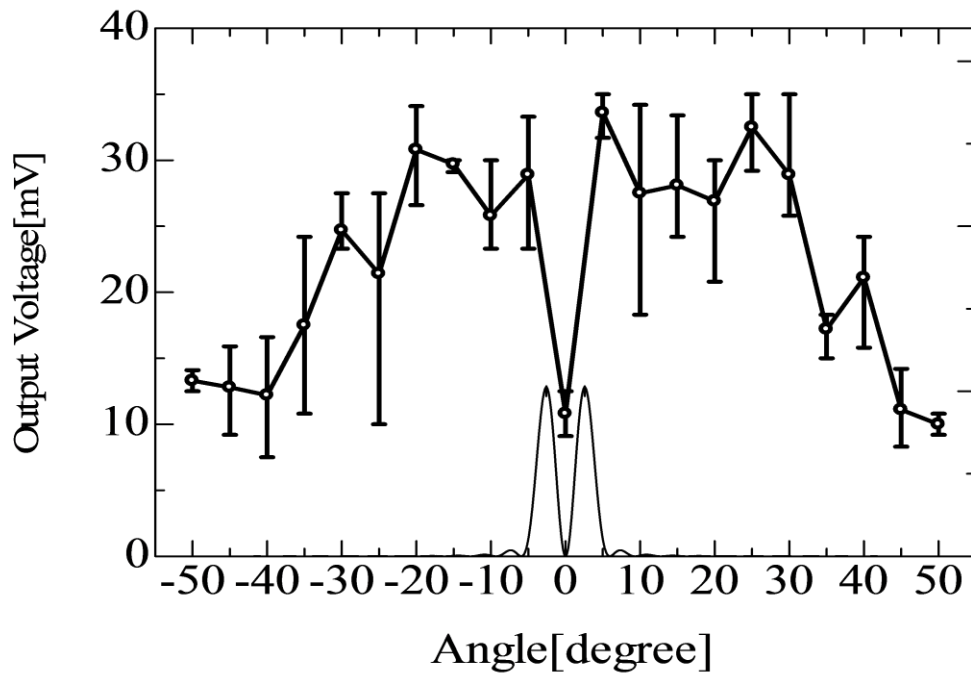


Fig. 4.17. Radiation pattern with the G-band BWO. G-band system is used and antenna distance from output window is 600 mm. A thin curve is theoretical curve of TM_{01} waveguide mode. (From Ref. 24)

straight waveguide section and radiate from the output window as shown in Fig. 4.11. Relationship between the excited CSWs and the radiation patterns spreading beyond 20 degree in Fig. 4.18 are still not clear. And more definite studies are required to understand details of excited CSWs in the resonator.

The radiation power is estimated using the D-band system. Considering 10 dB or 20dB attenuation provided in the detecting system, the maximum detected power levels are roughly evaluated to be in the range from some W to 10 W level. By integrating detected powers over the broad radiation pattern, the total radiation power is estimated to be in kW level.

4.6 Summary and Discussion

Weakly relativistic oversized BWOs using the waveguide type SWS have been studied in the K-, Q- and G-bands. These BWOs are driven by an annular electron beam with energy less than 100 keV. The radiation powers are up to about 500 and 200 kW for the K- and Q-band BWOs, respectively [10]. In this work, intense radiations on the order of 10 kW are obtained for the G-band BWO. For these BWOs, there exists a starting energy. Above the starting energy, intense radiations of oversized BWOs ranging from the K-band to the G-band are realized with

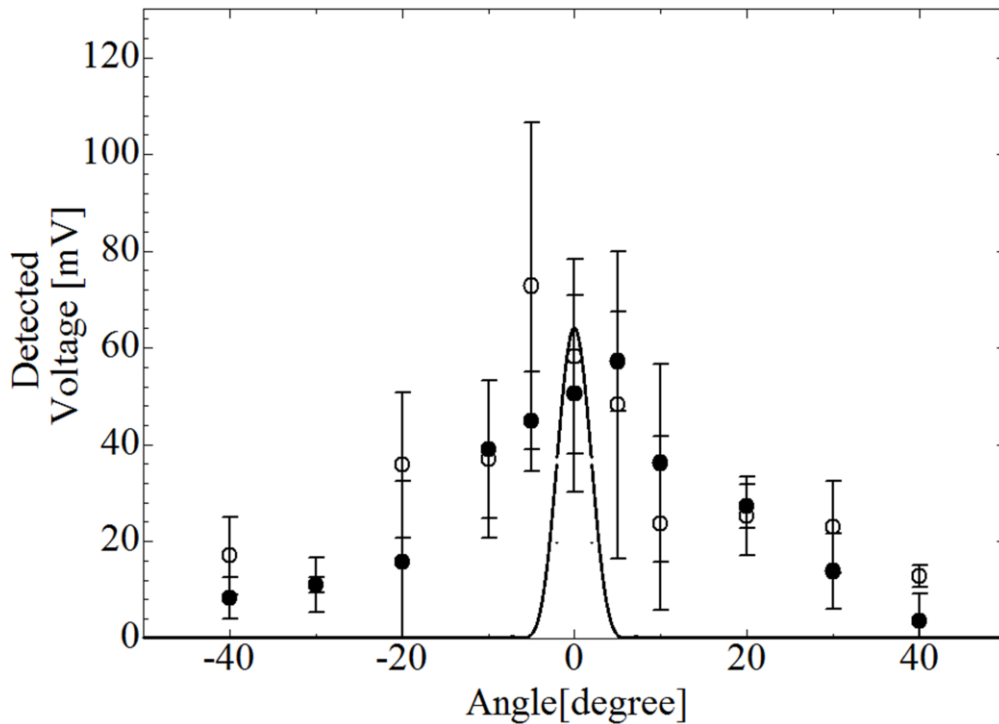


Fig. 4.18. Radiation pattern with the A-type G-band CSW-resonator. G-band detecting system is used and antenna distance from output window is 600 mm. Closed circles and open circles represent horizontal (E_θ) and vertical (E_ϕ) components of the electric field, respectively. The solid curve is theoretical radiation curve of TE_{11} waveguide mode. (From Ref. 62)

a very high figure of merit Pf^2 of about 3.5×10^2 [$MW \cdot GHz^2$]. Fig. 4.19 shows the relation of the radiation power and the oscillation frequency and the figure of merit Pf^2 for G-band BWO is presented in Fig. 4.19 with red closed circle. The figures of merit Pf^2 for non-oversized X-BWO and oversized K-, Q-BWO are also present in the figure with black closed circles, and distributed on a straight line $Pf^2 = 3.5 \times 10^2$ [$MW \cdot GHz^2$]. In future, the oscillations for 1 THz and several hundred watts can be expected. These oversized BWO operations are based on the global instability rather than the absolute instability. Also we demonstrate intense terahertz radiations based on the CSW-resonator above the starting energy. The starting energy is attributed to the axial modes imposed by the finite length of SWS and exists for the CSW-resonator as well as the waveguide type BWOs. The figure of merit Pf^2 for the CSW-resonator is calculated by using the detected output power and the operation frequencies. In Fig. 4.15, above starting energy the maximum detected power level for A-type corrugated cylinder is roughly evaluated to be about 10 W. By integrating detected powers over the broad radiation pattern as shown in Fig. 4.18, the total radiation power is estimated to be about 5 kW.

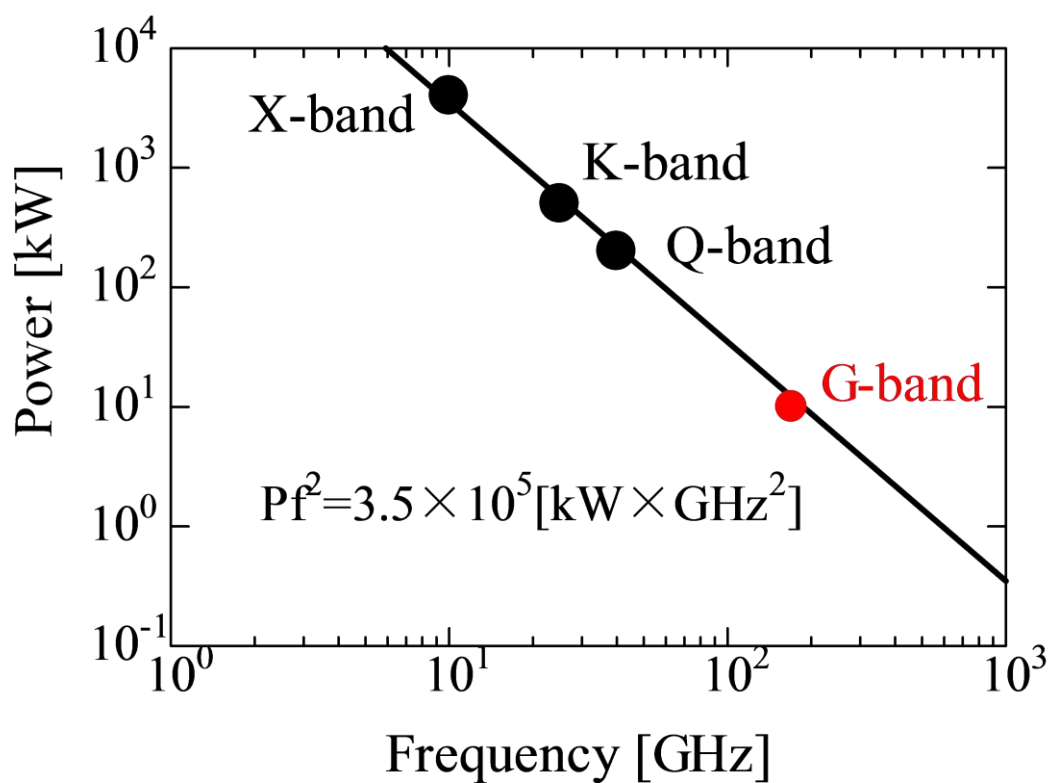


Fig. 4.19. The relation of the radiation power and the oscillation frequency.

And the operation frequency is 170 GHz as shown in Fig. 2.12 which is consistent with the experimentally obtained frequency range. With these values, the figure of merit Pf^2 is estimated to be about 1×10^2 [MW · GHz²] which is several times lower than the waveguide type oversized BWOs. However, the radiation power is in kW level and very intense radiations in terahertz regions are available using the CSW-resonator.

5 THEORETICAL AND EXPERIMENTAL STUDIES ON STARTING ENERGY AND CURRENT FOR OSCILLATION

5.1 Starting Energy for Oscillation

5.1.1 Numerical analysis and estimation of the starting energy for G-band BWO oscillation

The periodic SWS used in this work consists of modular sections having a rectangularly corrugated wall. The radial boundary conditions at the corrugation wall connect the frequency f and the axial wavenumber k_z by the dispersion relation

$$D(f, k_z) = 0. \quad (5.1)$$

For a finite-length BWO, the axial boundary conditions caused by the reflection at both ends should be considered as schematically shown in Fig. 5.1(a) [53]-[55]. In Fig. 5.1(a), k_z^- and k_b are the wavenumbers of the backward electromagnetic and beam modes, respectively. R_1 is the reflection coefficient at the beam entrance and R_2 is that at the other end. The beam interaction taking the effects of reflection into account can be expressed by the following equations.

$$D(f, k_b) = 0 \quad (5.2)$$

$$D(f, k_z^-) = 0 \quad (5.3)$$

$$R_1 R_2 \exp\{-i(k_z^- - k_b)L\} = 1. \quad (5.4)$$

Equation (5.4) is derived from the requirement that the field must be a single value at any axial position after one round trip of the field. The instability of the beam interaction for a finite L satisfying (5.2) to (5.4) is not the absolute instability predicted for the case of an infinite L . In Ref. 56, this instability is referred to as a “global instability”. In the limit of infinite L , k_b and k_z^- coincide and form a saddle point, resulting in oscillation due to an absolute instability. For finite L , however, an oscillation satisfying the axial boundary conditions does not occur at the saddle point.

For oscillations in the finite-length BWO, two thresholds are imposed from the real and

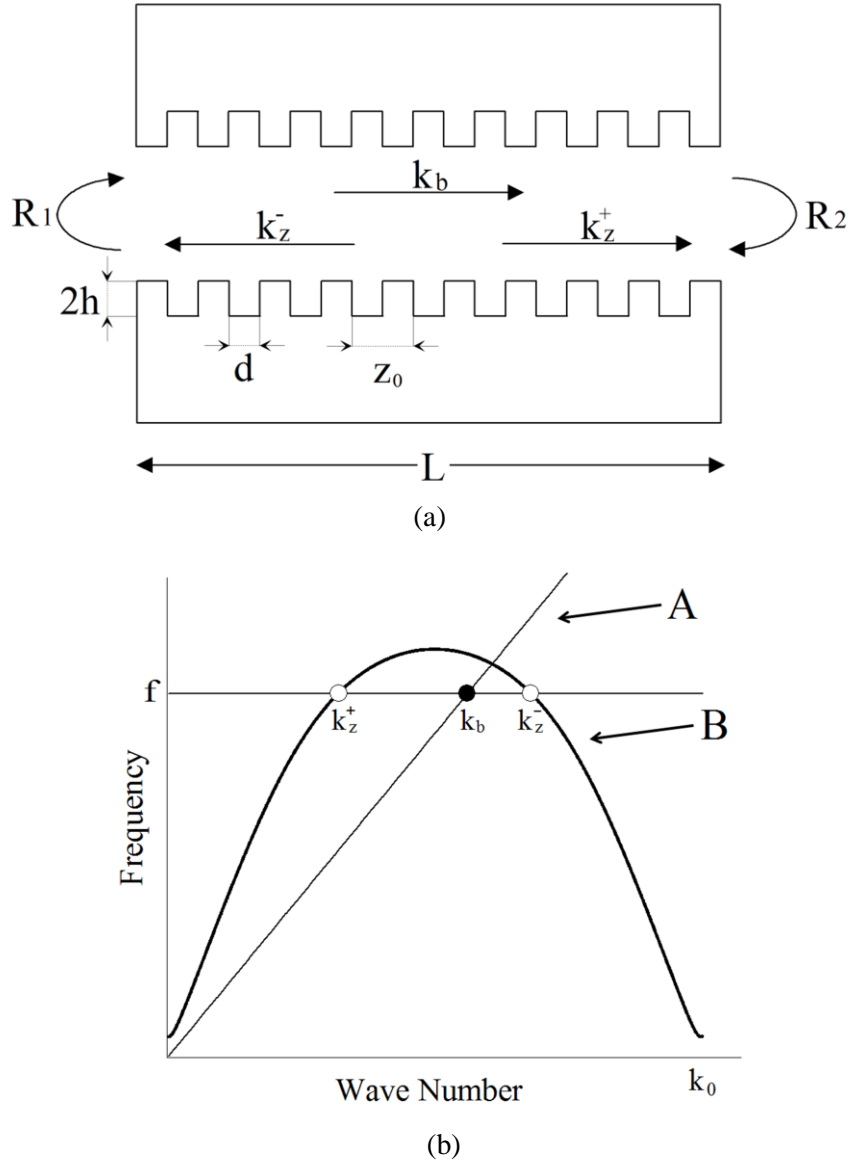


Fig. 5.1. Beam mode and forward and backward electromagnetic modes are represented by their wavenumbers k_b , k_z^+ , and k_z^- , respectively. The effects of reflection are taken into account using the reflection coefficients R_1 and R_2 . (a) Modes in SWS with finite length L and the parameters of the corrugations. (b) Schematic of width of global instability $\Delta k'_z$, where $\Delta k'_z$ is defined by (5.5). (From Ref. 61)

imaginary parts of (5.4). The imaginary part mainly determines the starting current. The real part of the width $\Delta k'_z$ of the global instability is given by

$$\Delta k'_z = R_e(k_z^- - k_b) = -\frac{2\pi N}{L}. \quad (5.5)$$

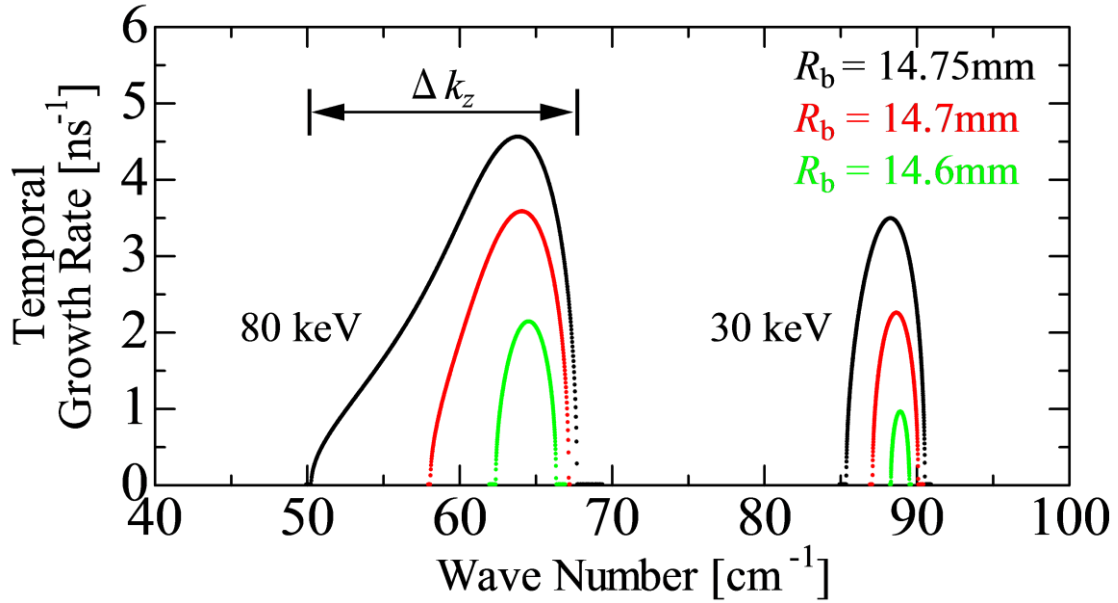


Fig. 5.2. Temporal growth rate versus oscillation wavenumber (From Ref. 61)

Here, N is an integer corresponding to the spatial harmonic of the periodic system, and the $N = -1$ harmonic is dominant over the other harmonics in the beam interaction. Note that both k_b and k_z are complex numbers and hence should be in the region of instability with width Δk_z in Fig. 5.2. The dispersion curves for G-band BWO in Fig. 2.11 are real number curves because the beam current is assumed to be zero. For a nonzero beam current, the beam interacts with the TM_{01} mode and the dispersion curves have imaginary parts corresponding to the growth rate of the TM_{01} mode. The beam interaction becomes stronger upon increasing the beam energy, because the beam power increases and the group velocity of the TM_{01} mode decreases approaching the π point. This can be seen from Fig. 5.2, which shows the temporal growth rates with a beam current of 200 A obtained using the numerical model in [57], [58]. The maximum growth rate for a beam energy of 80 keV is larger than that for a beam energy of 30 keV with the same beam radius R_b . The beam energy affects not only the maximum growth rate but also the width Δk_z of the instability (interaction width). For clarity, Δk_z in Fig. 5.2 is shown for a beam energy of 80 keV and $R_b = 14.75$ mm, and clearly depends on the beam energy. The growth rate is also affected by R_b . The R_b dependence may originate from the field properties in the oversized BWO, which are considerably different from those in a non-oversized BWO. The slow-wave becomes concentrated in the vicinity of the wall of the oversized BWO and decays sharply away from the wall. Hence, the growth rate becomes strong as the beam approaches the wall of the BWO, and both Δk_z and the peak value of the instability increase as can be seen from Fig. 5.2. In other words, a global instability with width $\Delta k'_z$ should be smaller than the

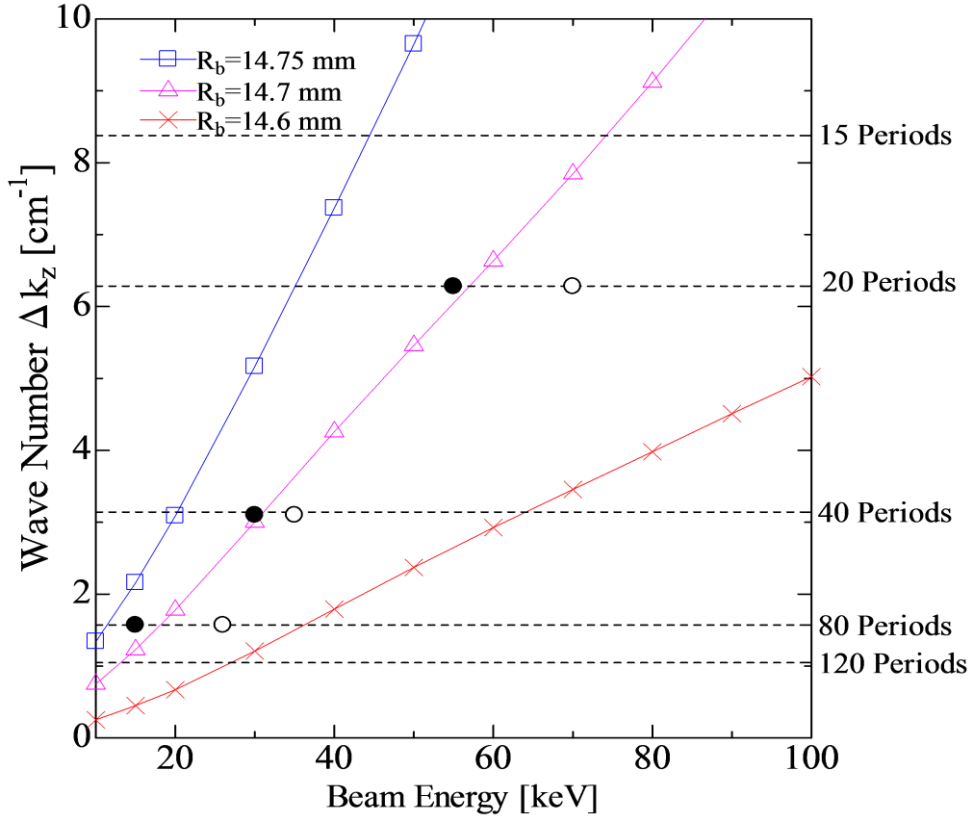


Fig. 5.3. Interaction width Δk_z versus beam energy with $R_b = 14.75$ mm (squares), 14.7 mm (triangles), and 14.6 mm (crosses). The dashed lines represent $2\pi/L$ for various L . Experimentally obtained starting energies with beam limiters of $\phi 29.5$ mm (white circles) and $\phi 29.7$ mm (black circles) are also plotted. (From Ref. 61)

interaction region with width Δk_z , i.e.,

$$\Delta k_z \geq \Delta k'_z. \quad (5.6)$$

In Fig. 5.1(b), the backward structure wave (shown by B) interacts with the beam mode (shown by A). The width $\Delta k'_z$ given by (5.5) is required for the global instability in a finite-length SWS, which is schematically shown in Fig. 5.1(b).

The frequency f of the global instability in Fig. 5.1(b) is determined so as to satisfy (5.5) subject to the finite length of the SWS. On the other hand, the width Δk_z of the instability in Fig. 5.2 is determined by the strength of the beam interaction, independently of the finite length of the SWS and condition of (5.6) cannot be satisfied by simply increasing the beam current as discussed in [54]. It is well known that beam-wave interactions are strong near the π point, where the group velocity of the backward structure wave becomes small. By increasing the

beam energy, the beam interaction point approaches the π point and Δk_z increases. At a critical beam energy, Δk_z satisfies (5.6) and a global instability with width $\Delta k'_z$ may occur. This is the reason for the existence of the minimum starting energy for oversized BWO oscillations.

The above statement is clarified in Fig. 5.3, where the numerically obtained Δk_z for the TM_{01} mode is shown assuming an infinitesimally thin annular beam with radius R_b [57], [58]. In Fig. 5.3, the values of R_b are 14.75, 14.7, and 14.6 mm with corresponding distances from the corrugation wall of 0.075, 0.125, and 0.225 mm, respectively. By increasing the beam energy, the interaction point approaches the upper cut off, i.e., the π point in Fig. 2.11, and Δk_z increases as can be seen in Fig. 5.3. At the critical beam energy, Δk_z may become sufficiently broad to satisfy (5.6). This critical beam energy is called the starting energy. The beam radius R_b strongly affects the beam interaction with the electromagnetic field near the tube wall, and Δk_z increases with increasing R_b as shown in Fig. 5.3.

In Fig. 5.3, lines representing $2\pi/L$, corresponding to the width $\Delta k'_z$ of the global instability, are plotted for different SWS lengths L . They cross the theoretical curves of Δk_z . The energy at the crossing point is the starting energy. If L is $40z_0$ (2 cm), then $2\pi/L$ is 3.14 cm^{-1} . In the case of $R_b = 14.7$ mm, the crossing occurs at about 30 keV. If the applied beam energy is larger than the starting energy, oscillation based on the global instability may be possible. In contrast, oscillation does not occur if the beam energy is lower than the starting energy. With increasing length L , the starting energy decreases because the dashed line becomes lower. It is emphasized, however, that the starting energy is a necessary condition for initiating the global instability. In the following, we experimentally show that this oscillation-starting condition is a sufficient one for the intense radiation of an oversized G-band BWO.

5.1.2 Numerical analysis and estimation of the starting energy for G-band CSW-resonator

The SWS-resonator used in this work is formed on a metal cylinder having a periodically corrugated wall. The radial boundary conditions at the corrugation wall connect the frequency f and the axial wavenumber k_z by the dispersion relation as shown in (5.1).

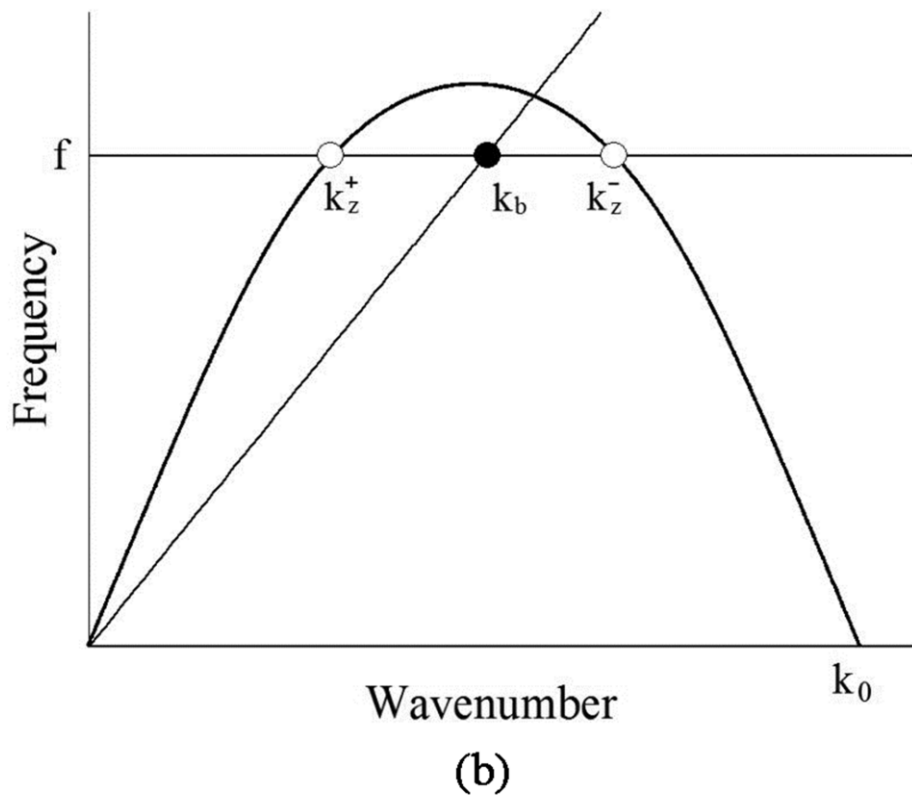
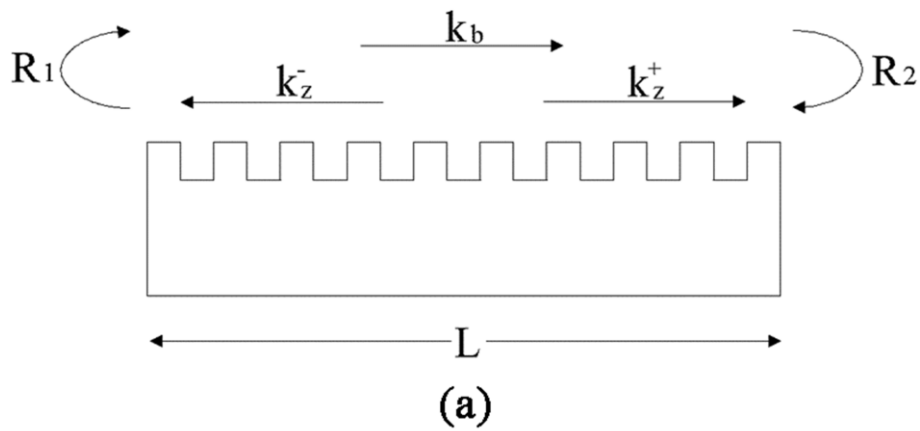


Fig. 5.4. Beam mode and forward and backward CSWs represent by their wavenumbers k_b , k_z^+ , and k_z^- , respectively. The effects of reflection are taken into account using the reflection coefficients R_1 and R_2 . (a) Modes in CSW-resonator with finite length L . (b) Schematic diagram of width of global instability $\Delta k_z'$, where $\Delta k_z'$ is defined by (5.5). (From Ref. 62)

When the beam current is zero, the dispersion curves obtained from (5.1) are real number curves of CSW as shown in Fig. 2.12. For a nonzero beam current, the beam modes are added

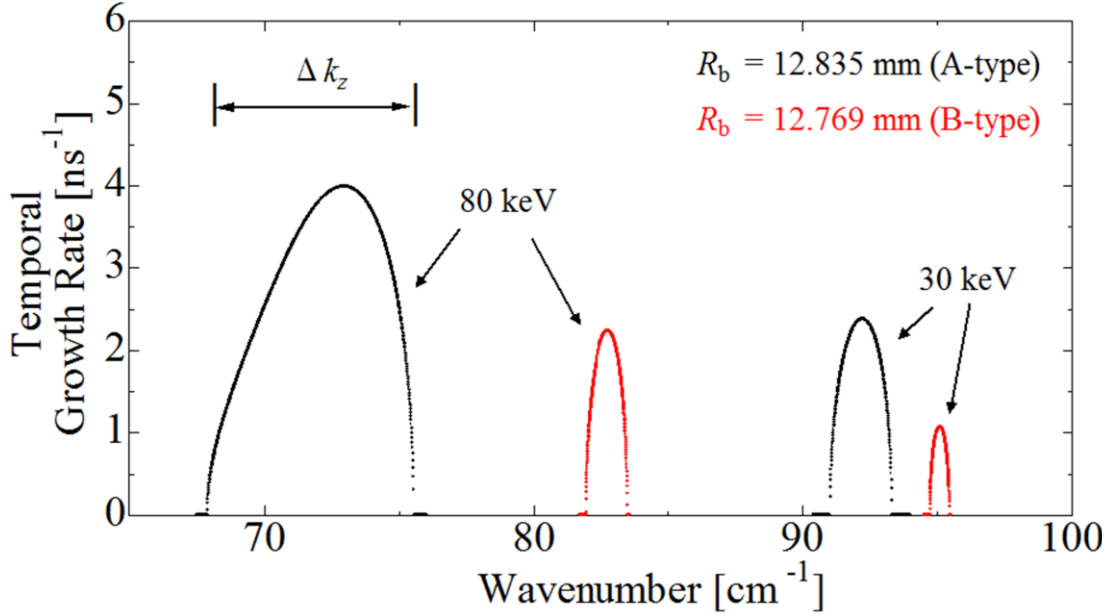


Fig. 5.5. Temporal growth rate versus oscillation wavenumber for a beam energy of 30 keV and 80 keV. Beam radii are 12.835 mm (A-type) and 12.769 mm (B-type), respectively. Beam current is 200A. (From Ref. 62)

and the dispersion curves have imaginary parts corresponding to the growth rate of the CSW. For the beam interaction in a finite-length CSW-resonator, the axial boundary conditions caused by the reflection at both ends should be considered as schematically shown in Fig. 5.4(a) [53]-[55]. In Fig. 5.4(a), k_z^+ , k_z^- and k_b are the wavenumbers of the forward CSW, backward CSW and beam mode, respectively. R_1 is the reflection coefficient at the beam entrance and R_2 is that at the other end. A BWO operation is realized for our CSW-resonator driven the weakly relativistic electron beams as shown in Fig. 2.12. The beam interaction with the backward CSW taking the effects of reflection into account can be expressed by (5.2) to (5.4).

Equation (5.4) is derived from the requirement that the field must be a single value at any axial position after one round trip of the field. The instability of the beam interaction for a finite L satisfying (5.2) to (5.4) is not the well-known absolute instability predicted for the case of an infinite L . In [56], this instability is referred to as a “global instability”. In the limit of infinite L , k_b and k_z^- coincide and form a saddle point, resulting in oscillation due to an absolute instability. For finite L , however, an oscillation satisfying the axial boundary conditions does not occur at the saddle point.

For oscillations in a finite-length CSW-resonator, two thresholds are imposed from the real and imaginary parts of (5.4). The imaginary part mainly determines the starting current. The real

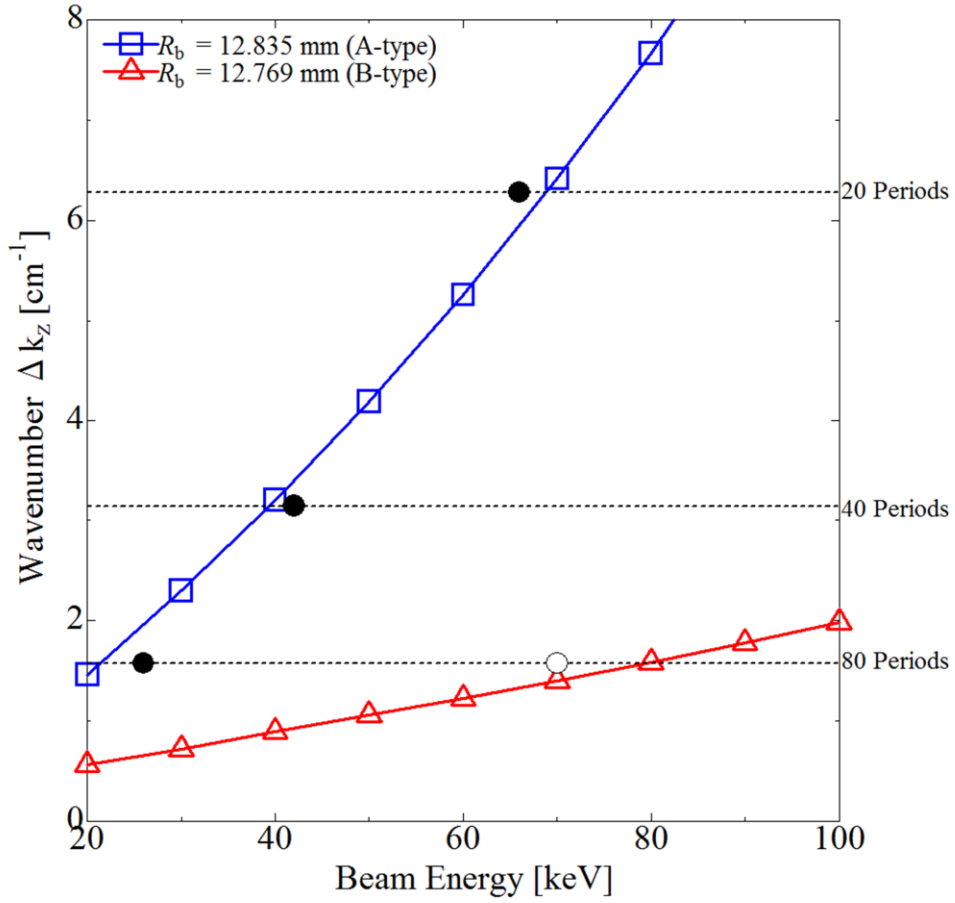


Fig. 5.6. Interaction width Δk_z versus beam energy with $R_b = 12.835$ mm (squares) and 12.769 mm (triangles). Beam current is 200A. The dashed lines represent $2\pi/L$ for various L . Experimentally obtained starting energies with the A-type CSW-resonator (black circles) and the B-type CSW-resonator (white circles) are also plotted. (From Ref. 62)

part of the width $\Delta k'_z$ of the global instability is given by (5.5).

Here, N is an integer corresponding to the spatial harmonic of the periodic system, and the $N = -1$ harmonic is dominant over the other harmonics in the beam interaction. Note that both k_b and k_z^- are complex numbers and hence should be in the region of instability with width Δk_z in Fig. 5.5, which shows the temporal growth rates with a beam current of 200 A obtained using the numerical model in [57], [58]. In other words, a global instability with width $\Delta k'_z$ should be smaller than the interaction region with width Δk_z as shown in (5.6).

In Fig. 5.4(b), the dispersion curve of CSW interacts with the beam mode. The width $\Delta k'_z$ given by (5.5) is required for the global instability in a finite-length CSW-resonator, which is schematically shown in Fig. 5.4(b). The frequency f of the global instability in Fig. 5.4(b) is

determined so as to satisfy (5.5) subject to the finite length of the CSW-resonator. The width Δk_z of the instability in Fig. 5.5 is determined by the strength of the beam interaction, independently of the finite length of the CSW-resonator and condition of (5.6) cannot be satisfied by simply increasing the beam current as discussed in [53], [54]. It is well-known that beam-wave interactions are strong near the π point, where the group velocity of the backward structure wave becomes small. By increasing the beam energy, the beam interaction point approaches the π point and Δk_z increases. At a critical beam energy, Δk_z satisfies (5.6) and a global instability with width $\Delta k'_z$ may occur. This is the reason for the existence of the minimum starting energy for surface wave oscillations.

The above statement is clarified in Fig. 5.6, where the numerically obtained Δk_z for the fundamental axisymmetric CSW is shown assuming an infinitesimally thin annular beam with radius R_b [57], [58]. In Fig. 5.6, the value of R_b is 12.835 mm (12.769 mm) with corresponding distance from the corrugation wall of 0.1 mm for the A (B)-type CSW-resonator. By increasing the beam energy, the interaction point approaches the upper cut off, i.e., the π point in Fig. 2.12, and Δk_z increases as can be seen in Fig. 5.5. In Fig. 5.6, lines representing $2\pi/L$, corresponding to the width $\Delta k'_z$ of the global instability, are plotted for different CSW-resonator lengths L . They cross the theoretical curves of Δk_z . The energy at the crossing point is the starting energy. If L is $40z_0$ (2 cm), then $2\pi/L$ is 3.14 cm^{-1} . In the case of $R_b = 12.835 \text{ mm}$ with the A-type CSW-resonator, the crossing point is at about 40 keV. If the applied beam energy is larger than the starting energy, oscillation based on the global instability may be realized. In contrast, intense oscillation does not occur if the beam energy is lower than the starting energy, where oscillations due to the absolute instability may dominate and relatively weak radiation realized. It is true that the conventional BWO operation based on the absolute instability generates intense stimulated radiations with the beam current above the starting current as reported in [20], [29]. The starting energy does not deny the BWO operation based on the absolute instability. It is a requirement for initiating oscillations in the finite length SWS with finite end reflections to form a CSW-resonator. With increasing the length L , the starting energy decreases because the dashed line ($\Delta k'_z$ given by (5.5)) in Fig. 5.6 becomes lower. Moreover, the starting energy increases when the corrugation amplitude h decreases from the A-type CSW-resonator to the B-type one, because the width Δk_z of the interaction region decreases as can be seen in Fig. 5.5.

5.2 Starting Current for Oscillation

5.2.1 Numerical analysis of starting current

The beam interaction considered is the Cherenkov interaction including three waves: the slow-space charge wave, the fast-space charge wave and the CSW. For an infinite length SWS,

the dispersion relation between the angular frequency ω ($=2\pi f$) and the axial wave number of the three-wave interaction may be expressed as [17],

$$(\delta\omega - v_b \delta k_z)^2 (\delta\omega - v_g \delta k_z) = \delta \quad (5.7)$$

Here, $\delta\omega = \omega - \omega_0$, $\delta k_z = k_z - k_{z0}$, v_b is the beam velocity, v_g is the group velocity. The parameter δ represents the effect of beam current and is written as

$$\delta = a^3 I_b, \quad (5.8)$$

where I_b is the beam current and a is determined for the three-wave interaction in a given SWS. The peak temporal growth rate of (5.7) occurs for $\delta k_z = 0$. With $\delta k_z = 0$, the three roots of $\delta\omega$ are given by

$$\delta\omega = \delta^{1/3}, \quad \delta^{1/3} \exp\left(i\frac{2\pi}{3}\right), \quad \text{and} \quad \delta^{1/3} \exp\left(-i\frac{2\pi}{3}\right). \quad (5.9)$$

And hence the peak temporal growth rate is

$$\max(\text{Im } \delta\omega) = \frac{\sqrt{3}}{2} \delta^{1/3} = \frac{\sqrt{3}}{2} a I_b^{1/3}. \quad (5.10)$$

Note that (5.7) is valid for the low current limit defined by the inequality

$$\left(\frac{\pi I_b}{\beta_b \gamma_b^3 I_A} \right)^{1/3} \ll 1, \quad (5.11)$$

where $\beta_b = v_b/c$, γ_b is the relativistic factor and $I_A = 17$ kA. In the low current limit, semi-analytical forms of δ have been derived for a planar SP-FEL [20], [29] and a cylindrical waveguide BWO [59]. Here, we evaluate δ using the value of a based on the numerical growth rate like Fig. 5.5. By changing I_b , the dependence of the peak temporal growth rate on I_b is numerically obtained.

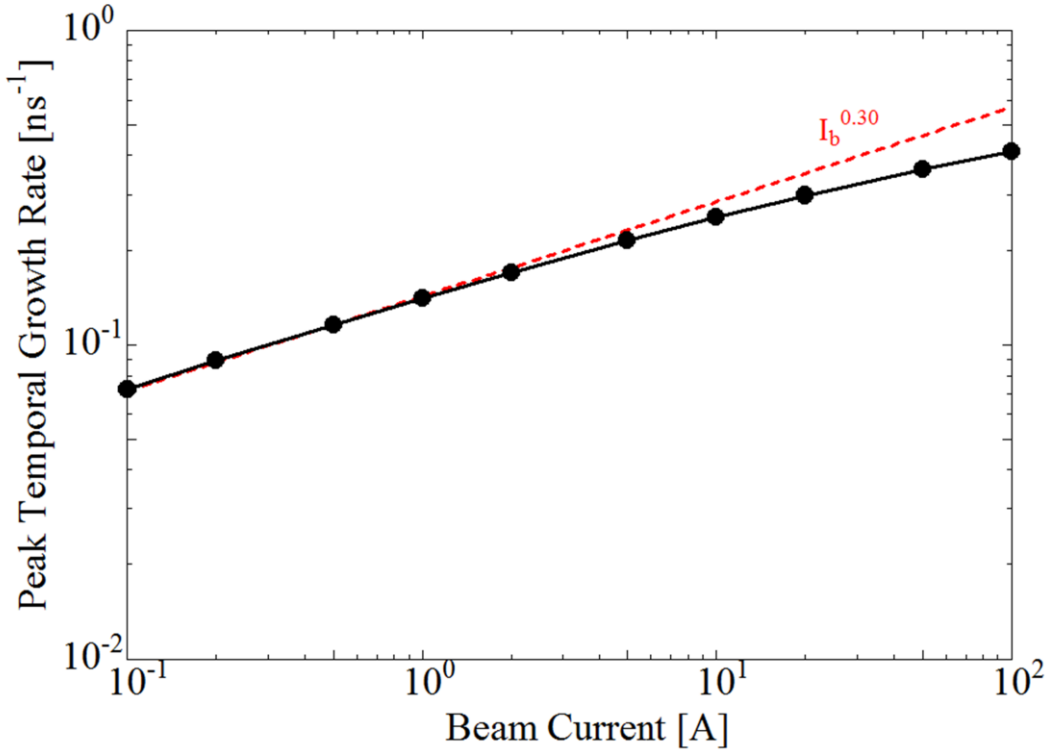


Fig. 5.7. Numerical peak temporal growth rates versus beam currents for oversized K-band BWO with the parameters average radius $R_0 = 15.7$ mm, pitch length $z_0 = 3.4$ mm, and corrugation amplitude $h = 1.7$ mm. The beam energy is 30 keV. (From Ref. 62)

5.2.2 Experiment of the starting current for K-band BWO oscillation

The dependence of the K-band BWO is shown in fig. 5.7 for later use. The peak temporal growth rate is approximately proportional to $I_b^{0.3}$ and fairly agrees with the $I_b^{1/3}$ scaling given by (14). The disagreement between $I_b^{0.3}$ and $I_b^{1/3}$ may be caused by the space charge effects of beam [58], [60]. The parameter a has a value of about 1×10^9 [1/(s · A^{1/3})] at 1 A for the case in Fig. 5.7.

For the starting current of a finite length BWO, three boundary conditions must be satisfied in addition to dispersion relation (5.7). The first two come from the requirement that the beam density and velocity perturbations vanish at the upstream end of the structure. The third condition is that there is no input field at the downstream end. Hence, the total axial electric field vanishes at the downstream end. As is pointed out in [59], the third condition may assume an idealized perfect match of the structure to an output, resulting in no reflection at the output end of the structure. Solving (5.7) subject to these boundary conditions, solutions different from an infinite length case given by (5.9) are obtained. And a threshold beam current exists, above which the imaginary part of $\delta\omega$ is positive. In [20], [59], the normalized current is defined as

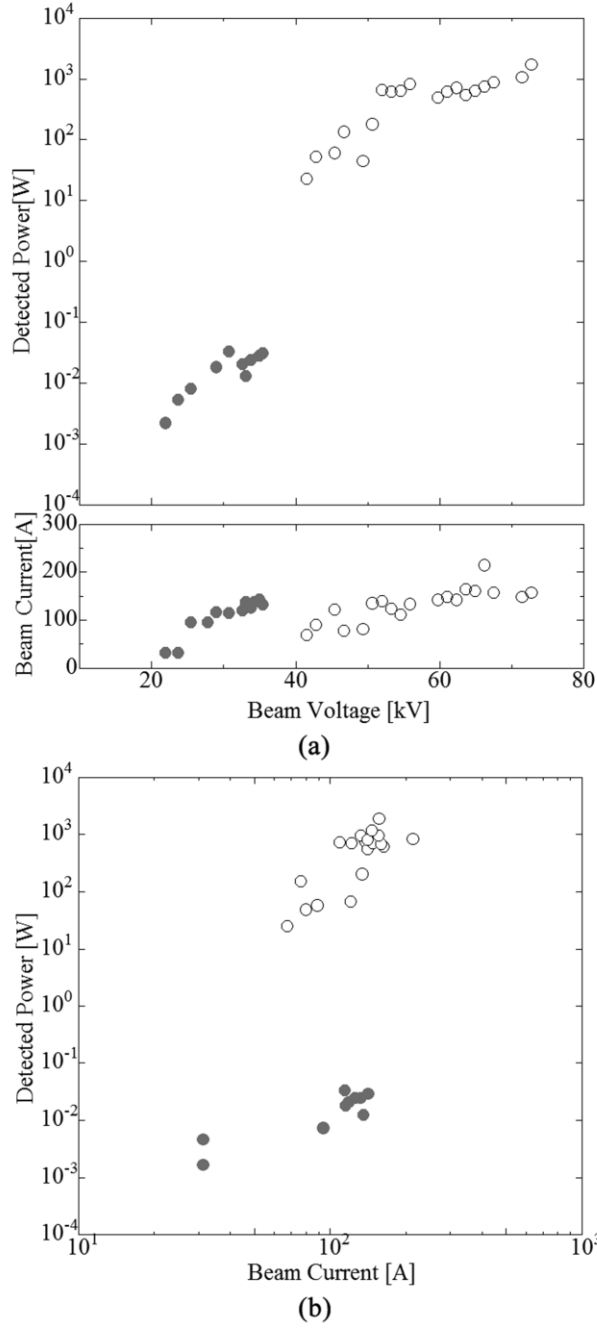


Fig. 5.7. (a) Detected power and beam current versus beam voltage for oversized K-band BWO with SWS length $L = 20z_0$. (b) The detected power is plotted as a function of the beam current for the oversized K-band BWO. Closed circles and open circles represent the operations above the starting current and starting energy, respectively. (From Ref. 62)

$$l = \left| \frac{\delta}{v_b v_g} \right| L^3 = \left| \frac{a^3 I_b}{v_b v_g} \right| L^3. \quad (5.12)$$

And its threshold value is found to be about 7.7. Hence, the starting current I_S is given by

$$I_S L^3 = \left| 7.7 \left(\frac{v_b}{a} \right)^2 \left(\frac{v_g}{a} \right) \right|. \quad (5.13)$$

To verify the starting current experimentally, we discuss operation of the oversized K -band BWO with $L = 20z_0$ presented in [53]. The detected power and the beam current are plotted in Fig. 5.8(a). And the detected power is plotted as a function of the beam current in Fig. 5.8(b). Radiations in mW level are observed around 20 kV and 30 A, and increases to tens mW level around 35 kV and 150 A. By increasing the beam voltage above 40 kV, radiations abruptly increase while the current is once decreases to about 60 A. This measurement required very careful operation of the BWO. Attenuation of typically 33dB was provided in the detecting system for the high-power detection above the starting energy. And all attenuations were removed for the low power detection. If the high-power was received without the attenuation around critical voltage, the detector would be seriously damaged. The abrupt microwave increase in Fig. 5.8(a) shows clearly the existence of the starting energy. Below the starting energy, the microwave signal is observed above about 30 A. By using the value of a in Fig. 5.7, the theoretical starting current derived from (5.13) is 28 A and reasonably agree with the experimental one. The double thresholds, i.e., the starting current and the starting voltage, are verified experimentally.

The starting currents of our G -band CSW-resonator are derived from (5.13) in the voltage region below the starting energy: 15A at 40 kV for the A-type with $L = 40z_0$ and 3 A at 60 kV for the B-type with $L = 80z_0$. The power above the starting current is expected to be much lower than that above the starting energy on the analogy of Figs. 5.8(a) and (b). Since the difference of detected power would be ten-thousand even hundred-thousand times, the detected power above the starting current for the G -band CSW-resonator would be less than 0.1 mW level which may be lower than the sensitivity of our detecting system in Fig. 4.11. For the starting current measurement of the G -band CSW-resonator, generated microwaves should be collected more effectively and our detection system should be made more highly sensitive. The starting current is proportional to L^{-3} . Hence, the operation current would become smaller as L increases. However, such L -dependence does not observed in Fig. 4.15, where the operation current seems to increase as L increases.

The starting energy is more critical than the starting current for the intense operation of the CSW-resonator. One essential difference between the starting current and the starting energy comes from the boundary condition at the upstream end of the structure. Zero R_2 at the output

end is assumed for the starting current, while a finite R_2 is involved for the starting energy. The reflectivity R_1 at the upstream end can have non-zero value for both starting thresholds. Although specific values of R_1 and R_2 are not obtained, these reflectivities may be large enough to form a resonator on the corrugated cylinder, which is called CSW-resonator in this paper. Formation of CSW-resonator has been demonstrated by using the metal cylinder with K -band corrugation on the surface [33], in which a K -band CSW-resonator was excited by needle antennas and the microwave reflection profile was measured by a network analyzer. Measured resonance curves show two kinds of CSW: the bounded surface wave and hybrid surface wave. The former may be responsible for the intense operation region of CSW-resonator, since the latter is too far from the π point to satisfy the starting energy. The experimental resonance curves show quality factors of the resonator on the order of hundreds for the bounded surface wave. These quality factors correspond to the total quality factor Q_T , which include the ohmic quality factor Q_Ω and the diffractive quality factor Q_d . Q_Ω is related to the power loss in the corrugation wall by resistive heating and Q_d is related to the power loss by diffraction at ends of the corrugation. The relationship between the resonator end-reflection and Q_d may be given as

$$R = \sqrt{\frac{1 - \alpha/Q_d}{1 + \alpha/Q_d}} \quad \text{and} \quad \alpha = \frac{\omega L}{v_g} \quad (5.14)$$

Here, R is the round trip reflectivity $R = R_1 \times R_2$. The three quality factors have the relation

$$\frac{1}{Q_T} = \frac{1}{Q_\Omega} + \frac{1}{Q_d} \quad (5.15)$$

The SWS is made of aluminum and its Q_Ω may be on the order of thousands. Hence, to explain the Q_T of hundreds order, Q_d should be on the order of hundreds, leading to the round trip reflectivity around some tens % or more for the K -band CSW-resonator. Nearly the same reflectivity might be expected for the G -band CSW-resonator, since the dispersion curves of the G -band CSW are located near to those of the K -band CSW if they are plotted in terms of the normalized frequency z_0/λ and the normalized wavenumber in units of k_0 .

5.3 Summary and Discussion

In this chapter, we examined the starting conditions for G -band BWO and CSW-resonator theoretically and experimentally. We found that an oscillation-starting energy exists for the oversized G -band BWO and CSW-resonator, below which meaningful radiation cannot be observed. The same starting energy defined by (5.5) has also been demonstrated for intense

radiation from the oversized K-band BWO in [53]. The starting energy is a more critical condition than the starting current for the intense operation of oversized BWOs. This oscillation condition is for the global instability and is peculiar to the finite-length SWS as mentioned in this chapter. From our theoretical study, we found that the starting current can be derived from the imaginary part of (5.4) rather than the real part. Also, the starting current may be determined from the balance between the input power from the beam and the power losses to the lossy walls and ends of the SWS. To compensate for the power losses, the beam current may be increased. However, no meaningful radiation was observed below the critical voltage, regardless of the amount of the beam current, within the limit of the pulse power system of about 800 A. The abrupt appearance of microwaves in Fig. 4.14 and Fig. 4.15 can be convincingly explained by (5.5). The experimentally obtained starting energy decreased with increasing L , as plotted in Fig. 5.3 and Fig. 5.6, which are in a good agreement with the theoretical prediction shown in Fig. 5.3 and Fig. 5.6 for the G-band BWO and CSW-resonator. Our CSW-resonator is a multimode system and non-axisymmetric CSWs exist very close to the axisymmetric CSW. They have almost the same dispersion characteristics in the beam interaction region. The beam interactions are the strongest for $m = 0$ and 1, weaken gradually with increasing m . Hence, their starting energies are almost the same as that of the axisymmetric CSW and increase by increasing m . If these CSWs do not interact non-linearly, the starting condition can be discussed representatively based on the dispersion curve of the lowest CSW with $m = 0$ like oversized K - and G -band waveguide type BWO. This work may properly demonstrate the oscillation starting condition for the oversized G-band BWO and CSW-resonator.

6 Conclusion

An oversized G-band BWO driven by a weakly relativistic electron beam with energy less than 100 kV was studied. Rectangular corrugations were used as the SWS, which had surface waves with upper cut off frequencies of above 150 GHz in the G-band. We examined the starting conditions for intense G-band BWO operation by varying the beam parameters and the SWS lengths. It was shown that a starting energy exists for the intense radiation of G-band BWO and that the starting energy is more critical than the starting current. Above the starting energy, very intense output powers on the order of 10 kW were obtained. The oversized G-band BWO presented in this study realized intense radiation with the same figure of merit as weakly relativistic BWO in the lower-frequency K- and Q-bands. The oscillation-starting condition for such intense operation may play an important role in high-intensity terahertz wave sources.

Intense terahertz radiations based on oversized CSW-resonator driven by an annular electron beam in weakly relativistic region less than 100 kV was also studied experimentally in this work. The beam was generated by a disk type cold cathode. The CSW-resonator was formed on a rectangularly corrugated metal cylinder. The sizes of fabricated corrugation were measured using a digital microscope. We designed two types of the corrugated cylinder with the different corrugation amplitude h , and the operation frequency ranges of 166-173 GHz and 182-200 GHz was demonstrated exciting the CSW-resonators by an annular electron beam. It was shown that a starting energy exists for the intense radiation of the CSW-resonator. The starting energy is attributed to the axial boundary conditions imposed by the finite length of SWS and exists for the CSW-resonator as well as the waveguide type BWOs. Above the starting energy, very intense output powers on the order of some kW were obtained. Measured radiation patterns illustrate that the oversized CSW-resonator is a multimode system. The figure of merit Pf^2 is about 1×10^2 [MW·GHz²], which is several times lower than the waveguide type BWOs. The terahertz CSW-resonator with such intense radiation power in the weakly relativistic region and artificial controllability of electromagnetic property may be of considerable interest for practical use and for developing compact terahertz wave sources.

REFERENCES

- [1] V. L. Granatstein and I. Alexeff, Ed., *High-Power Microwave Sources*, Dedham, MA: Artech House, 1987.
- [2] J. Benford and J. A. Swegle, *High Power Microwaves*, Boston, MA: Artech House, 1992.
- [3] A. V. Gaponov-Grekhov and V. L. Granatstein, Ed., *Applications of High-Power Microwaves*, Boston, MA: Artech House, 1994.
- [4] K. R. Chu and H. L. Hirshfield, "Comparative Study of the Axial and Azimuthal Bunching Mechanisms in Electromagnetic Cyclotron Instabilities", *Phys. Fluids*, vol. 21, no. 3, pp. 461-466, Mar. 1978.
- [5] C. J. Edgcombe, "Gyrotron Oscillators", Taylor & Francis, London, 1993.
- [6] R. Kompfner, "Backward-wave oscillator", *Bell Lab. Rec.*, vol. 31, pp. 281-285, 1953.
- [7] Y. Carmel, et al., "Intense coherent Cherenkov radiation due to the interaction of a relativistic electron beam with a slow-wave structure", *Phys. Rev. Lett.*, vol. 33, no. 21, pp. 1278-1282, 1974.
- [8] V. S. Ivanov, et al., "Investigation of a relativistic Cerenkov self-generator", *Sov. Phys. Tech. Phys.*, vol. 23, no. 5, pp. 580-583, 1981.
- [9] A. N. Vlasov, A. G. Shkvarunets, J. C. Rodgers, Y. Carmel, T. M. Antonsen, T. M. Abuefadi, D. Lingze, V. A. Cherepenin, G. S. Nusinovich, M. Botton, and V. L. Granatstein, "Overmoded GW-class surface-wave microwave oscillator," *IEEE Trans. Plasma Sci.*, vol. 28, pp. 550-560, Jun. 2000.
- [10] S. Aoyama, Y. Miyazawa, K. Ogura, A. Sugawara, and M. Hirata, "Improved performance of oversized backward wave oscillator driven by weakly relativistic electron beam," *Fusion Sci. Technol.*, vol. 51, pp. 325-327, Feb. 2007.
- [11] S. P. Bugaev, V. A. Cherepenin, V. I. Kanavets, V. I. Koshelev, V. A. Popov and A. N. Vlasov, "Investigation of a millimeter-wavelength-range relativistic diffraction generator," *IEEE Trans. Plasma Sci.*, vol. 18, pp. 518-524, Jun. 1990.
- [12] S. P. Bugaev, V. A. Cherepenin, V. I. Kanavets, A. I. Klimov, A. D. Kopenkin, V. I. Koshelev, V. A. Popov and A. I. Slepikov, "Relativistic multiwave Cherenkov generators," *IEEE Trans. Plasma Sci.*, vol. 18, pp. 525-536, Jun. 1990.
- [13] K. Ogura, Y. Miyazawa, S. Aoyama, Y. Takamura, S. Tamura and A. Sugawara, "Studies of a weakly relativistic oversized backward wave oscillator with disk cathode and rectangular corrugation," *IEEJ Trans. FM.*, vol. 127, pp. 681-686, Nov. 2007.
- [14] S. J. Smith and E.M. Purcell, "Visible Light from Localized Surface Charges Moving across a Grating", *Phys. Rev.* Vol. 92, p.1069, 1953.

- [15] F. S. Rusin and G. D. Bogomolov, "Orotron—an electron oscillator with an open resonator and reflecting grating", Proc. IEEE., vol. 57, pp. 720–722, Apr. 1969.
- [16] K. Mizuno, S. Ono and Y. Shibada, "Two different mode interactions in an electron tube with a Fabry-Perot resonator-The Ledatron", IEEE Transactions on Electron Devices, vol. 20, pp. 749-752, Aug. 1973.
- [17] J. R. Pierce, *Travelling-wave Tubes*. D. Van Nostrand Company, Inc., New York, Jul. 1950.
- [18] A. V. Gunin et al., "Relativistic X-band BWO with 3-GW output power", IEEE Transactions on Plasma Science, vol. 26, p. 326, Jun. 1998.
- [19] J. Urata, M. Goldstein, M.F. Kimmitt, A. Naumov, C. Platt and J.E. Walsh, "Superradiant Smith-Purcell Emission", Phy. Rev. Lett. Vol. 80, no. 3, pp.516-519, Jan. 1998.
- [20] V. Kumar and K. -J. Kim, "Analysis of Smith-Purcell free-electron lasers", Phys. Rev. E 73, 026501, Feb. 2006.
- [21] C. A. Florya, "Analysis of Super-Radiant Smith-Purcell Emission", J. Appl. Phys. vol. 99, 054903, Mar. 2006.
- [22] H. L. Andrews, C. A. Brau, and J. D. Jarvis, "Observation of THz Evanescent Waves in a Smith-Purcell Free-Electron Laser", Phys. Rev. ST Accel. Beams Vol. 12, 080703, Aug. 2009.
- [23] V. L. Bratman, A. E. Fedotov, and P. B. Makhalov, "Experimental Demonstration of Smith-Purcell Radiation Enhancement by Frequency Multiplication in Open Cavity", Appl. Phys. Lett. vol. 98, 061503, Feb. 2011.
- [24] S. Magori, K. Ogura, T. Iwasaki, J. Kojima, K. Yambe, S. Kubo, T. Shimosuma, S. Kobayashi, and K. Okada, "Experimental Study on G-Band oversized Backward Wave Oscillator Driven by Weakly Relativistic Electron Beam", Plasma Fusion Res., vol. 9, 3406032, Apr. 2014.
- [25] K. Ogura, K. Yambe, H. Yoshimura, and M. Takahashi, "Experimental Study on Backward Wave Oscillation Based on Cylindrical Surface Wave of Smith-Purcell Free Electron Laser", Plasma Fusion Res., vol. 6, 2401039, Jul. 2011.
- [26] S. Hasegawa, K. Ogura, T. Iwasaki, and K. Yambe, "Smith-Purcell Radiation Based on Cylindrical Surface Waves", Fusion Sci. Technol., vol.63, no.1T, pp.259-261, May 2013.
- [27] J. B. Pendry, L. Martin-Moreno, and F. J. Garcia-Vidal, "Mimicking Surface Plasmons with Structured Surfaces", Science, vol. 305, no.6, pp.847-848, Aug. 2004.
- [28] C. R. Williams, S. R. Andrews, S. A. Maier, A. I. Fernandez-Dominguez, L. Martin-Moreno, and F. J. Garcia-Vidal, "Highly Confined Guiding of Terahertz Surface

- Plasmon Polaritons on Structured Metal Surfaces”, *Nature Photonics*, vol. 2, pp.175-179, Mar. 2008.
- [29] H. L. Andrews, J. D. Jarvis, and C. A. Brau, “Three-dimensional theory of the Smith–Purcell free-electron laser with side walls”, *J. Appl. Phys.* vol. 105, 024904, Jan. 2009.
- [30] S. A. Maier, S. R. Andrews, Martin-Moreno, and F. J. Garcia-Vidal, “Terahertz Surface Plasmon-Polariton Propagation and Focusing on Periodically Corrugated Metal Wires”, *Phys. Rev. Lett.*, vol. 97, 176805, Oct. 2006.
- [31] K. Ogura, K. Yamamoto, Y. Kobari, and K. Yambe, “Cylindrical Surface Wave and Slow-Wave Instabilities of Periodically Corrugated Cylinder”, *Fusion Sci. Technol.*, vol.63, no.1T, pp.152-155, May 2013.
- [32] W. Main, Y. Cannel, K. Ogura, J. Weaver, G. S. Nusinovich, S. Kobayashi, J. P. Tate, J. Rodgers, A. Bromborsky, S. Watanabe, M.R. Amin, K. Minami, W.W. Destler, and V.L. Granatstein “Electromagnetic Properties of Open and Closed Overmoded Slow-Wave Resonators for Interaction with Relativistic Electron Beams,” *IEEE Trans. Plasma Sci.*, vol. 22, no.5, pp.566-576, Oct. 1994.
- [33] K. Ogura, H. Iiduka and K. Yambe, “Cylindrical Surface Wave on Periodically Corrugated Metal Cylinder”, *Plasma Fusion Res.*, vol. 7, 2406022, Mar. 2012.
- [34] T. I. Jeon, J. Zhang, and D. Grischkowsky, “THz Sommerfeld Wave Propagation on a Single Metal Wire”, *Appl. Phys. Lett.* vol. 86, no.16, 161904, Apr. 2005.
- [35] M. Mineo and C. Paoloni, “Double Corrugation Rectangular Waveguide Slow-wave Structure for THz Vacuum Devices”, *IEEE Trans. on Electron Devices*, vol. 57, no.11, pp. 3169-3175, Nov. 2010.
- [36] W. He, L. Zhang, D. Bowes, H. Yin, K. Ronald, A. D. R. Phelps, and A. W. Cross, “Generation of broadband terahertz radiation using a backward wave oscillator and pseudospark-sourced electron beam”, *Appl. Phys. Lett.*, vol. 107, 133501, Sep. 2015.
- [37] M. Y. Glyavin, A. G. Luchinin, and G. Y. Golubiatnikov, “Generation of 1.5-kW, 1-THz coherent radiation from a gyrotron with a pulsed magnetic field”, *Phys. Rev. Lett.*, vol. 100, no. 1, p. 015101, Jan. 2008.
- [38] T. Idehara, T. Saito, H. Mori, H. Tsuchiya, L. Agusu, and S. Mitsudo, “Long pulse operation of the THz gyrotron with a pulse magnet”, *Int. J. Infrared Millim. Waves*, vol. 29, no. 2, pp. 131-141, Feb. 2008.
- [39] V. L. Bratman, Y. K. Kalynov, and V. N. Manuilov, “Large-orbit gyrotron operation in the terahertz frequency range”, *Phys. Rev. Lett.*, vol. 102, no. 24, p. 245101, Jun. 2009.
- [40] V. L. Bratman, B. S. Dumesh, A. E. Fedotov, P. B. Makhlov, B. Z. Movshevich, and F. S. Rusin, “Terahertz Orotrons and Oromultipliers”, *IEEE Trans. Plasma Sci.*, vol. 38, no. 6, pp. 1466-1470, Jun. 2010.

- [41] L. R. Elias, V. Jaccarino, and W. M. Yen, "Scientific research with the UCSB free-electron laser", Nucl. Instrum. Methods Phys. Res. A, Accel. Spectrom. Detect. Assoc. Equip., vol. 239, no. 3, pp. 439-442, Sep. 1985.
- [42] N. G. Gavrilov, B. A. Knyazev, E. I. Kolobanov, V. V. Kotenkov, et al., "Status of the Novosibirsk high-power terahertz FEL", Nucl. Instrum. Methods Phys. Res. A, Accel. Spectrom. Detect. Assoc. Equip., vol. 575, no. 1/2, pp. 54-57, May 2007.
- [43] R. M. Bevensee, "Electromagnetic Slow Wave Systems", John Wiley & Sons Inc., New York, 1994.
- [44] V. I. Aronov, L. S. Bogdankevich, and A. A. Rukhadze, Sov. Phys. Tech. Phys., vol. 18, p. 452, 1973.
- [45] L. S. Bogdankevich and A. A. Rukhadze, Sov. Phys. Tech. Phys., vol. 22, p. 145, 1977.
- [46] John A. Pasour in *High Power Microwave Sources*, edited by V. L. Granatstein and I. Alexeff, Dedham, MA: Artech House, p.207, 1987.
- [47] P. J. B. Clarricoats and A. D. Olver, *Corrugated Horns for Microwave Antennas*, London: Peter Peregrinus Ltd, IEE, 1984.
- [48] S. A. Maier, S. R. Andrews, Martin-Moreno, and F. J. Garcia-Vidal, "Terahertz Surface Plasmon-Polariton Propagation and Focusing on Periodically Corrugated Metal Wires", Phys. Rev. Lett., vol. 97, 176805, Oct. 2006.
- [49] R. J. Barker and E. Schamiloglu, *High-Power Microwave Sources and Technologies*. Piscataway, NJ, USA: IEEE Press, 2001, ch.9.
- [50] O. T. Loza and I. E. Ivanov, "Measurement of the angular spectrum of electrons in a high-current magnetized REB with microsecond duration", in *Proc. 13th Int. Conf. High-Power Particle Beams*, pp. 603-606, Jun. 2000.
- [51] D. M. Pozar, *Microwave Engineering*, 2nd ed, New York: John Wiley & Sons, Inc., 1998, p. 706.
- [52] Y. Kiuchi, H. Tanaka, K. Ogura, O. Watanabe, T. Cho, and Md. R. Amin, "Slow cyclotron and Cherenkov instabilities in weakly relativistic oversized backward wave oscillator", Fusion Sci. Technol., vol. 51, no.2T, pp. 331-333, Feb. 2007.
- [53] K. Ogura, R. Yoshida, Y. Yamashita, H. Yamazaki, K. Komiyama and M. Sakai, "Study on oscillation starting condition of K-band oversized backward wave oscillator driven by a weakly relativistic electron beam," J. Plasma Fusion Res. Ser., vol. 6, pp. 703-706, Mar. 2004.
- [54] K. Minami, K. Ogura, Y. Aiba, M. R. Amin, X. D. Zheng, T. Watanabe, Y. Carmel, W. W. Destler, and V. L. Granatstein, "Starting energy and current for a large diameter finite

- length backward wave oscillator operated at the fundamental mode,” IEEE Trans. Plasma Sci., vol. 23, pp. 124-132, Apr. 1995.
- [55] K. Minami, M. Mortuza Ali, K. Ogura, W. Kim, and T. Watanabe, “Analysis of starting currents in a backward wave oscillator with finite structure length,” J. Phys. Soc. Jpn., vol. 61, no. 10, pp. 3566-3575, Oct. 1992.
- [56] E. M. Lifshitz and L. P. Pitaevskii, Physical Kinetics, New York: Pergamon Press, 1981, pp. 281-283.
- [57] K. Ogura, K. Yambe, K. Yamamoto, and Y. Kobari, “Normal modes and slow-wave instabilities in oversized coaxial slow-wave structure with rectangular corrugations,” IEEE Trans. Plasma Sci., vol. 41, pp. 2729-2734, Oct. 2013.
- [58] K. Ogura, A. Kojima, F. Kawabe, K. Yambe, and Md. R. Amin, “Surface waves in oversized G-band slow-wave structures with rectangular corrugations,” Plasma Fusion Res., vol. 9, 3406022, Mar. 2014.
- [59] J. A. Swegle, “Starting conditions for relativistic backward wave oscillators at low currents”, IEEE Trans. Plasma Sci., vol. 30, pp. 1201-1211, Apr. 1987.
- [60] H.P. Freund, “A Re-Examination of the Traveling Wave Interaction”, IEEE Trans. Plasma Sci., vol. 22, no.5, pp.499-503, Oct. 1994.
- [61] S. Gong, K. Ogura, S. Nomizu, A. Shirai, K. Yamazaki, K. Yambe, S. Kubo, T. Shimozuma, S. Kobayashi, and K. Okada, “Oscillation-Starting Conditions for Oversized G-Band (140-220 GHz) Backward Wave Oscillator Driven by a Weakly Relativistic Electron Beam”, IEEE Trans. Plasma Sci., vol. 43, no. 10, pp. 3530-3536, Oct. 2015.
- [62] S. Gong, K. Ogura, K. Yambe, S. Nomizu, A. Shirai, K. Yamazaki, J. Kawamura, T. Miura, S. Takanashi, and Min Thu San, “Experimental Study of Intense Radiation in Terahertz Region based on Cylindrical Surface Wave Resonator”, J. Appl. Phys., vol. 118, no. 12, 123101, Sep. 2015.
- [63] R. B. Miller, “Mechanism of explosive electron emission for dielectric fiber (velvet) cathodes”, J. Appl. Phys., vol. 84, pp. 3880-3889, Jul. 1998.